**Accepted manuscript.** Published in Journal of the Mechanics and Physics of Solids (2026). Version of record: https://doi.org/10.1016/j.jmps.2026.106660. © 2026. This manuscript version is made available under the CC-BY-NC-ND 4.0 license https://creativecommons.org/licenses/by-nc-nd/4.0/

# On the Yielding of Brittle Granular Materials at Elevated Temperatures

Yazeed Kokash[1], Richard Regueiro[2], Yida Zhang[3*]

## Abstract

Environmental conditions such as temperature and humidity majorly affect the mechanical properties of geomaterials such as stiffness, strength and time-dependent behavior (e.g., creep, relaxation, time-to-failure). Modeling the thermomechanical responses of geomaterials is becoming increasingly important, driven by the rising demand for environmentally-secure nuclear-waste repositories, efficient deep-geothermal energy extraction, and climate-resilient geostructures. In this study, we seek to mechanistically link temperature-dependent macroscopic yielding in brittle granular materials to the temperature dependence of the surface energy of their constituent solids. We begin by modeling the surface energy $\gamma$ of minerals such as quartz by examining the intermolecular potential and its variability with respect to temperature. We then upscale this property to the continuum description of brittle granular assemblies through a novel surface-based breakage mechanics theory (SBM), in which the specific surface area $A_s$ is the sole internal state variable tracking the degree of crushing in the granular matrix. An advantage of this choice is that $A_s$ and $\gamma$ naturally form a thermodynamically conjugated pair, allowing $\gamma$ and its temperature dependency to explicitly appear in the yield function of the granular material. The surface-area growth law is obtained from a grain size distribution (GSD) with an evolving fractal dimension, supported by X-ray tomography data on crushable granular materials. The derived model successfully predicts the

[1] PhD student, Department of Mechanical Engineering, University of Colorado Boulder, Boulder, Colorado, USA.
[2] Professor, Department of Civil, Environmental and Architectural Engineering, University of Colorado Boulder, Boulder, Colorado, USA
[3] Associate Professor, Department of Civil, Environmental and Architectural Engineering, University of Colorado Boulder, Boulder, Colorado, USA.
*Corresponding author: yida.zhang@colorado.edu

temperature-dependent yielding and stress-strain behavior of both consolidated and unconsolidated sands over temperatures from 20 °C to 150 °C, relying solely on the knowledge of surface energy variations at the mineral scale. These results support the hypothesis that, within the tested temperature range, thermal weakening is governed predominantly by reductions in solid surface energy, while changes in the elastic and hardening properties of the granular materials play at most a secondary role.

**Keywords**: granular materials, yielding, thermal weakening, surface energy, grain breakage.

## 1. Introduction

The mechanical properties of materials such as stiffness, strength, and time-dependent behaviors (e.g., creep, stress relaxation, time-to-failure) are greatly affected by environmental conditions (e.g., humidity and temperature) (Chester et al., 2007; Chester et al., 2004; Heap et al., 2009; Karner et al., 2008; Paterson and Wong, 2005; Wong, 1982). This holds true for geomaterials above and below Earth's surface, where they are exposed to constantly changing or cyclic thermal conditions driven by natural causes and human activities. Understanding the effect of temperature on the behavior of geomaterials is important for engineering applications such as underground nuclear waste disposal (Gens et al., 2009), geothermal energy extraction (Duggal et al., 2022; Gkousis et al., 2022), and climate-change adaptation of geostructures (Brandl, 2006). Daily and seasonal temperature fluctuation also accelerates rock weathering and impacts the morphology of our landscapes (Buckman et al., 2021; Eppes and Keanini, 2017; Monahan et al., 2025).

The effect of temperature on the mechanical and fracture behavior of rocks and sands has been investigated under various experimental settings including triaxial compression (Heap et al., 2009; Jefferd et al., 2021; Karner et al., 2008), creep (Kranz et al., 1982; Niemeijer et al., 2002; Punya-in and Kongkitkul, 2023), and fracture toughness and crack velocity measurements (Darot et al., 1985; Meredith and Atkinson, 1982). Darot et al. (1985) measured the surface energy for olivine and quartz single crystals using micro-indentation technique for the temperature range between 20 and 900 °C. For both minerals, the surface energy decreases with increasing temperature up to a certain critical temperature $T_c$ which is around 500 °C for olivine and 573 °C for quartz corresponding to the $\alpha-\beta$ phase transition. The surface energy above $T_c$ stays almost the same for olivine but increases significantly and reaches a plateau at 900 °C for quartz. Meredith and Atkinson (1982) conducted subcritical crack propagation experiments on synthetic

47 quartz crystals at different temperatures (up to 300 °C) in vacuum and under water vapor pressures (up to
48 300 Pa) using a double torsion setup. In both vacuum and humid conditions, temperature had a major
49 influence on the crack velocity - stress intensity factor ($v_c - K_I$) curves: for a given $K_I$, $v_c$ increased by
50 about 5 orders of magnitude as temperature rose from 20 to 200 °C. Karner et al. (2008) conducted
51 isotropic and triaxial compression tests on St. Peter quartz sand at various temperatures. For isotropic
52 loading, increasing the temperature from 24 °C to 150 °C resulted in a 10% increase in porosity reduction
53 and a 12% rise in the number of acoustic emissions (AE) at a 55 MPa effective confining pressure. The
54 impact of temperature on triaxial loading is similar. It was observed that the reduction of the yield strength
55 at elevated temperature is more pronounced at high confinement while negligible at low confinement.
56 Jefferd et al. (2021) reported similar findings on Bleursville, Locharbriggs, and Boise sandstones through
57 triaxial compression tests conducted at room temperature and 150 °C under effective confining pressure
58 of up to 120 MPa. Heap et al. (2009) performed creep experiments on Bentheim, Darley Dale, and Crab
59 Orchid sandstones with AE monitoring at room temperature and 75 °C. They found that axial strains and
60 porosity changes exhibited typical trimodal creep behavior at both temperatures, with elevated
61 temperatures significantly increasing the creep strain rate by several orders of magnitude. Collectively,
62 these studies suggest that the reduced yield strength of brittle granular materials may be attributed to the
63 thermal enhancement of crack growth and grain breakage at microscale.

64 Modeling wise, many elastoplastic theories have been developed to account for the effect of temperature
65 on the yield envelope of geomaterials (Hueckel et al., 1994; Liu et al., 2020; Xing et al., 2020). In these
66 models, thermal weakening is introduced by prescribing empirical temperature dependencies for the
67 yielding and hardening parameters, thereby controlling the size and the evolution rate of the yield surface.
68 While this approach can achieve satisfactory agreements with experimental observations, it lacks a
69 micromechanical foundation, and its consistency with the second law of thermodynamics remains

questionable. In this regard, the continuum breakage mechanics theory (CBM) (Einav, 2007a, b) presents a compelling alternative to the conventional elastoplastic approach for modeling brittle granular materials. CBM is entirely derived from a free energy potential and an non-negative dissipation potential, thus inherently complies to thermodynamic principles (Houlsby and Puzrin, 2007). It tracks the grain size evolution through a breakage variable, $B$, which elegantly establishes micromechanical linkages between gradation and the granular system's energy storage and dissipation. Recently, we proposed a non-isothermal extension of CBM (Kokash et al., 2024) that captures the pressure-, rate-, and temperature-dependent behavior of plastic-bonded granular materials. Among the model parameters, the critical breakage energy $E_C$ which governs the size of the yield surface exhibited the greatest sensitivity with respect to temperature. Taken together with prior theoretical and experimental evidence that $E_C$ is tightly linked to the fracture properties of single grains (Sohn et al., 2017; Zhang et al., 2016; Zhou et al., 2019), it is plausible that the observed temperature dependence of $E_C$ arises from the thermal effects on the fracture toughness $K_C$, or equivalently the surface energy $\gamma$, of the grain minerals. Indeed, as shown by Zhang and Buscarnera (2018), the commonly observed water weakening of sands and rockfills is naturally reproduced by augmenting CBM with an $E_C$ - $\gamma$ relation, combined with the Gibbs adsorption isotherm to predict the humidity-dependent reduction of $\gamma$.

In this context, this paper seeks to mechanistically link the macroscopic yielding of brittle granular materials to the surface energy of the constituent solid, and to test the hypothesis that the reduced yield strength at elevated temperatures is primarily attributable to reductions in surface energy. We begin in Section 2 by examining the fundamentals of temperature-dependent surface energy of solids, where we attribute the temperature effect to variations in their intermolecular potentials. Sections 3 details a novel surface-based breakage mechanics theory. Departing from Zhang and Buscarnera (2018) where surface

area $A_s$ served only as an intermediate quantity, we take $A_s$ as the sole internal state variable (ISV) in place of $B$ to characterize the collective crushing of the granular matrix. This allows the surface energy $\gamma$ (the thermodynamic conjugate to $A_s$) and its environmental variations to explicitly appear in the free energy and dissipation potentials of the granular system, enabling the prediction of temperature-dependent clastic yielding based on mineralogical knowledge. To preserve gradation tracking and its micromechanical implications, $A_s$ is mapped to the grain size distribution (GSD) which evolves fractally from the initial to an ultimate GSD, providing a more realistic representation of the accumulation of fines compared with the linear interpolation adopted in the original CBM. The model's performance is assessed in Section 4 against thermomechanical experimental datasets for sandstones and sands. Finally, Section 5 provides some concluding remarks and future prospectives.

## 2. Thermal weakening at mineral scale

### *2.1. Thermodynamics of crack growth*

Let us begin by considering a simple two-dimensional particle containing a line crack at the center as illustrated in Figure 1. The particle is positioned between two displacement-controlled loading plates and immersed in a surface-adsorbing fluid containing $k$ number of species, with both fluid volume and composition independently controlled. Differing from our previous derivation (Zhang and Buscarnera, 2018), the system considered here is in equilibrium with a heat reservoir whose temperature $T$ can be varied. External rate of work can be input to the system through three independent controls: displacing the top plate, changing the fluid volume, and altering moles of individual species:

$$\dot{W} = F\dot{\Delta} + P\dot{V}^f + \sum_{i=1}^{k} \mu_i \dot{N}_i \tag{1}$$

where $F$ is the compressive force; $\Delta$ the displacement of the top platen; $P$ the fluid pressure; $V^f$ the fluid volume; $\mu_i$ and $N_i$ the chemical potential and the total number of moles of species $i$ in the system. Fluid species can exist either in the bulk fluid or adsorbed onto the exposed solid surfaces including cracks and boundary:

$$N_i = N_i^f + N_i^{surf} = N_i^f + 2\Gamma_i l \tag{2}$$

where superscripts $f$ and $surf$ denote the bulk fluid and the surface excess phases, respectively; $\Gamma_i$ is the number of adsorbed mole of species $i$ per unit length on the crack; $l$ is the crack length with two sides.

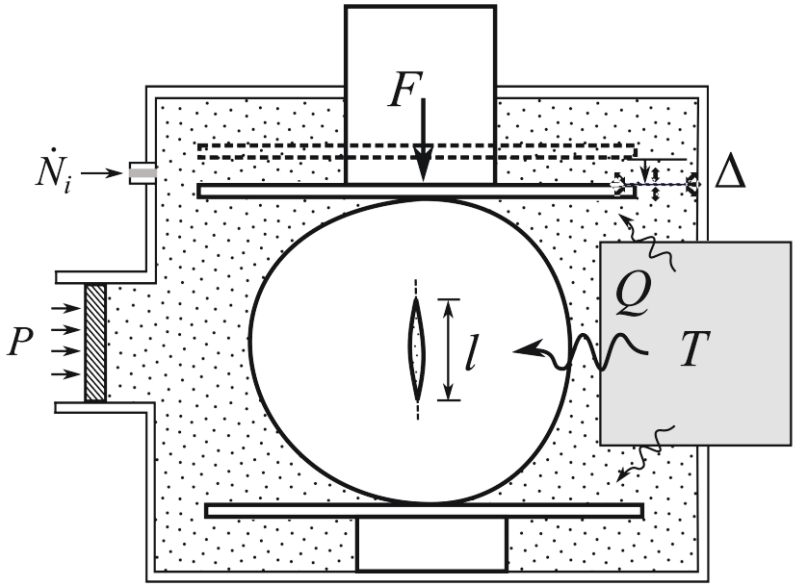


Figure 1: Schematic diagram of a particle with a crack immersed in a fluid environment and the temperature can vary, modified from Zhang and Buscarnera (2018).

The first and second laws of thermodynamics state that:

$$\dot{U} = \dot{W} + Q\,;\ \dot{S} = \frac{Q}{T} + \Lambda, \Lambda \geq 0 \tag{3}$$

where $U$ is the total internal energy in the system; $Q$ is the rate of heat supply; $S$ is the entropy; $\Lambda$ is the non-negative entropy production rate. The free energy imbalance of the system is obtained by combining Eqs. (1) and (3):

$$F\dot{\Delta} + P\dot{V}^f + \sum_{i=1}^{k} \mu_i \dot{N}_i - S\dot{T} - \dot{\Psi} = T\Lambda \geq 0 \tag{4}$$

where $\Psi = U - ST$ is the Helmholtz free energy. The total Helmholtz free energy and entropy can be decomposed into contributions related to the solid, the fluid, and the surface excess phases as:

$$\Psi = \Psi^s + \Psi^f + 2\psi^{surf} l \tag{5}$$

$$S = S^s + S^f + 2s^{surf} l \tag{6}$$

where $\psi^{surf}$ and $s^{surf}$ are respectively the free energy and entropy of the interface per unit length. We further propose that the free energy stored in each phase depends solely on the kinematics of that phase: the solid Helmholtz free energy depends on the displacement, the length of the internal flaw, and temperature $\Psi^s = \Psi^s\left(\Delta, l, T\right)$; that of the fluid is controlled by its composition, volume, and temperature $\Psi^f = \Psi^f\left(N_1^f, ..., N_k^f, V^f, T\right)$; and the surface phase is characterized by the adsorbed excess and temperature $\psi^{surf} = \psi^{surf}(\Gamma_1, ..., \Gamma_k, T)$. The increment of total Helmholtz free energy is therefore given by:

$$\dot{\Psi} = \underbrace{\left[\frac{\partial \Psi^s}{\partial \Delta}\dot{\Delta} + \frac{\partial \Psi^s}{\partial l}\dot{l} + \frac{\partial \Psi^s}{\partial T}\dot{T}\right]}_{\dot{\Psi}^s} + \underbrace{\left[\frac{\partial \Psi^f}{\partial V^f}\dot{V}^f + \sum_{i=1}^{k}\frac{\partial \Psi^f}{\partial N_i^f}\dot{N}_i^f + \frac{\partial \Psi^f}{\partial T}\dot{T}\right]}_{\dot{\Psi}^f} + 2\underbrace{\left[\psi^{surf}\dot{l} + \sum_{i=1}^{k}\frac{\partial \psi^{surf}}{\partial \Gamma_i}\dot{\Gamma}_i l + \frac{\partial \psi^{surf}}{\partial T}\dot{T}l\right]}_{\dot{\psi}^{surf} l} \tag{7}$$

Substituting Eq. (7) into Eq. (4) gives:

$$\Phi^s + \Phi^f + 2l\phi^{surf} = T\Lambda \geq 0 \tag{8}$$

where

$$\Phi^s = \left( F - \frac{\partial \Psi^s}{\partial \Delta} \right) \dot{\Delta} + \left[ -\frac{\partial \Psi^s}{\partial l} + 2\left( \sum_{i=1}^{k} \mu_i \Gamma_i - \psi^{surf} \right) \right] \dot{l} + \left( -S^s - \frac{\partial \Psi^s}{\partial T} \right) \dot{T} \tag{9}$$

$$\Phi^f = \left( P - \frac{\partial \Psi^f}{\partial V^f} \right) \dot{V}^f + \sum_{i=1}^{k} \left( \mu_i - \frac{\partial \Psi^f}{\partial N_i^f} \right) \dot{N}_i^f + \left( -S^f - \frac{\partial \Psi^f}{\partial T} \right) \dot{T} \tag{10}$$

$$\phi^{surf} = \sum_{i=1}^{k} \left( \mu_i - \frac{\partial \psi^{surf}}{\partial \Gamma_i} \right) \dot{\Gamma}_i + \left( -s^{surf} - \frac{\partial \psi^{surf}}{\partial T} \right) \dot{T} \tag{11}$$

are dissipation rates related to the solid, the fluid, and the interface, respectively. Assuming reversible processes such that the dissipation is zero ( $\Phi^s = \Phi^f = l\phi^{surf} = 0$ , $\dot{l} = 0$ ), the following relations can be obtained:

$$F = \frac{\partial \Psi^s}{\partial \Delta};\ P = \frac{\partial \Psi^f}{\partial V^f};\ \mu_i = \frac{\partial \Psi^f}{\partial N_i^f} = \frac{\partial \psi^{surf}}{\partial \Gamma_i};\ S^s = -\frac{\partial \Psi^s}{\partial T};\ S^f = -\frac{\partial \Psi^f}{\partial T};\ s^{surf} = -\frac{\partial \psi^{surf}}{\partial T} \tag{12}$$

A new surface potential $\gamma$ can be introduced through Legendre transform of $\psi^{surf}$ :

$$\gamma \equiv \psi^{surf}\left(\Gamma_i, T\right) - \sum_{i=1}^{k} \Gamma_i \mu_i \tag{13}$$

Substituting (13) and (12) into (9) and considering general processes $\Phi^s \geq 0$ retrieves the celebrated Rice's criterion for crack growth and healing (Rice, 1978):

$$\left(G - 2\gamma\right)\dot{l} \geq 0 \tag{14}$$

where $G \equiv -\partial \Psi_s / \partial l$ is the energy release rate. Eq. (14) also reveals that the physical meaning of $\gamma$ is essentially the solid-fluid surface energy that controls the onset of crack growth. Combining the rate form of Eq. (13) and Eq. (12) gives the non-isothermal Gibbs adsorption relation:

$$\dot{\gamma} = -\sum_{i=1}^{k} \Gamma_i \dot{\mu}_i - s^{surf} \dot{T} \tag{15}$$

Eq. (15) suggests that, thermodynamically, surface energy of the solid must depend on both the chemical composition of the surrounding fluid and the temperature of system, i.e., $\gamma = \gamma\left(T, \mu_1, ..., \mu_k\right)$. Environment-dependent surface energy, and consequently fracture toughness, is a key mechanism through which factors like humidity and temperature influence the mechanical behavior of brittle geomaterials. Zhang and Buscarnera (2018) explored the effect of humidity on the yielding of sand and rockfills under isothermal conditions and demonstrated that incorporating water adsorption on mineral surface $\gamma = \gamma\left(\mu_w\right)$ allows quantitative predictions of water weakening effect. In this work, we shall focus on the effect of temperature on surface energy $\gamma = \gamma\left(T\right)$ by maintaining constant fluid environment ($\dot{\mu}_i = 0$), and explore the subsequent macroscopic effects.

### *2.2. Temperature-dependency of surface energy*

One way to construct an expression for $\gamma = \gamma\left(T\right)$ is to integrate Gibbs relation Eq. (15). However, unlike adsorption isotherms $\Gamma_i\left(\mu_i\right)$ which are routinely measured for solid-fluid interfaces, data on surface entropy $s^{surf}\left(T\right)$ is typically unavailable. Alternatively, we seek atomistic explanations of the temperature dependency of $\gamma$ in this subsection. According to Rice's criterion (14), propagating a crack requires the elastic energy released from solid body overcomes twice of the surface energy (if other dissipation mechanism such as plasticity are neglected). At the atomic level, crack propagation can be understood as

the sequential rupture of bonds, overcoming the attractive interatomic forces as the separation increases from the equilibrium position ($w = w_0$) to infinity along the propagation path (see Fig. 2). Comparing the two perspectives, it is straightforward to see that the energy input per unit crack length to rupture the bonds is exactly equivalent to the macroscopic energy threshold, $2\gamma$. This provides a way to connect surface energy and characteristics of the equivalent interatomic potential. Orowan (1949) and Gilman (1960) were among the first to adopted this approach to calculate the theoretical strength and surface energy of crystal by approximating the force-separation relationship with a half-sinusoidal function. Here, we adopt a similar approach but with the following innovations: 1) instead of using a highly idealized half-sine function, we will use a more realistic functional representation of the interatomic forces; 2) we focus on the dependency of the surface energy with temperature.

Among the many pair potential models, the Morse potential is a simple and yet effective choice suitable for brittle materials with mostly dominant covalent bonds (Wiederhorn, 1969). Its expression is given by:

$$U(w) = U_0\left[e^{-2a(w-w_0)} - 2e^{-a(w-w_0)}\right] \tag{16}$$

where $U_0$ is the depth of the energy potential; $a$ is a parameter with units of 1/length, which is inversely related to the interaction range or decay length (Kelly, 1966); $w$ represents the interatomic distance, with $w_0$ denoting its value at equilibrium. The interatomic force is given by:

$$F(w) = \frac{\partial U}{\partial w} = 2aU_0\left[e^{-a(w-w_0)} - e^{-2a(w-w_0)}\right] \tag{17}$$

which is positive for attraction. A schematic representation of the Morse potential and the corresponding force is shown in Figure 2.

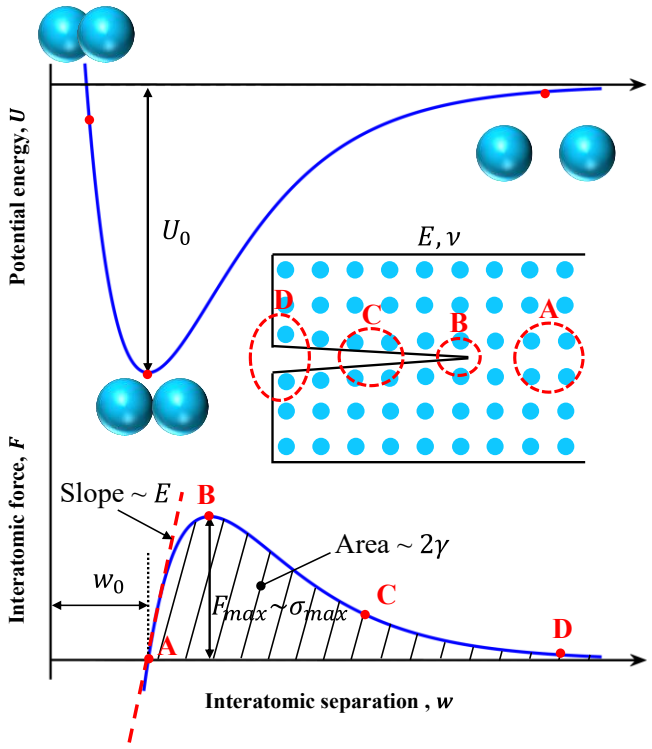


Figure 2: Schematic representation of the Morse potential and the corresponding interatomic force, highlighting the conceptual link between the force–separation curve and the solid's elastic and fracture properties.

The cohesive stress $\sigma$ between two planar solid surfaces is essentially the interatomic forces smeared over a unit area (or length for 2D case). It is plausible to assume proportionality between the two

$$\frac{F}{F_{max}} = \frac{\sigma}{\sigma_{max}} \tag{18}$$

where $F_{max}$ and $\sigma_{max}$ are the maximum attraction force and cohesive stress, respectively. $F_{max}$ can be found by setting the derivative of Eq. (17) with respect to $w$ to zero:

$$F_{max} = \frac{U_0 a}{2} \tag{19}$$

Combining (17), (18) and (19) gives the equation for the cohesive stress:

$$\sigma(w) = 4\sigma_{max}\left[e^{-a(w-w_0)} - e^{-2a(w-w_0)}\right] \tag{20}$$

Eq. (20) is essentially a 3-parameter stress-separation model. The benefit of this simplicity is that key macroscopic properties of the bulk solid can be expressed in terms of interatomic parameters. For example, assuming periodic atomic structure, the slope of the $\sigma(w)$ curve around equilibrium $w_0$ can be equate to the apparent Young's modulus of the solid (Kelly, 1966):

$$E = w_0 \left.\frac{\partial\sigma}{\partial w}\right|_{w=w_0} \tag{21}$$

, revealing a linkage between $\sigma_{max}$ and $E$ by:

$$\sigma_{max} = \frac{E}{4aw_0} \tag{22}$$

Similarly, the area underneath the $\sigma(w)$ curve represents the energy per unit area required to completely separate the two solid surfaces and is linked to $\gamma$ though (Kelly, 1966; Lawn, 2010):

$$2\gamma = \int_{w_0}^{\infty} \sigma(w)\,\mathrm{d}w \tag{23}$$

Substituting Eq. (20) into (23) and considering (22) gives:

$$\gamma = \frac{E}{4a^2w_0} \tag{24}$$

A more commonly reported property from fracture experiments is the fracture toughness $K_{IC}$, which under plane strain conditions is related to surface energy by Irwin's relation:

$$2\gamma = \frac{K^2{}_{IC}(1-\nu^2)}{E} \tag{25}$$

where $\nu$ is the Poisson's ratio. Substituting (24) gives:

$$K_{IC} = \frac{E}{\sqrt{2w_0\left(1-\nu^2\right)}}\frac{1}{a} \tag{26}$$

Eq. (24) or (26) provides a useful way to estimate surface energy based on the knowledge of Young's modulus, Poisson's ratio, decay length, and equilibrium interatomic distance of the solid. To focus our discussion on the temperature dependency, it is possible to normalize (24) or (26) with respect to their values at a reference temperature $T^r$:

$$\frac{\gamma(T)}{\gamma^r} = \frac{E(T)}{E^r}\frac{w_0^r}{w_0(T)}\left(\frac{a^r}{a(T)}\right)^2 \tag{27}$$

$$\frac{K_{IC}(T)}{K_{IC}^r} = \frac{E(T)}{E^r}\sqrt{\frac{w_0^r\left(1-\nu^{r2}\right)}{w_0(T)\left(1-\nu(T)^2\right)}}\frac{a^r}{a(T)} \tag{28}$$

where the superscript "$r$" denotes reference values. In writing Eqs. (27) and (28), we have assumed that the elastic modulus, Poisson's ratio, decay parameter $a$, and equilibrium separation $w_0$ are functions of temperature. The variation of the elastic modulus and Poisson's ratio with temperature has been measured and reported in numerous laboratory studies for different mineral crystals. On the other hand, the dependency of parameters $a$ and $w_0$ warrants some discussion. In principle, temperature is a macroscopic property reflecting the average kinetic energy of the particles or the severity of atomic 'jiggling', and thus is defined at a scale larger than interatomic distances. Nevertheless, researchers sometimes incorporate temperature directly into interatomic descriptions to capture macroscopic thermomechanical behaviors of

the solid (Nasehzadeh et al., 2002). For example, in the work of Sutton (1989), the total free energy is decomposed into a configurational (interatomic) term plus a vibrational (phonon) term that depends on temperature. Taking derivatives of this free energy yields an effective, temperature-dependent interatomic force. In the same spirit, the current work captures the effect of temperature on the lattice structure and interatomic force by allowing the potential parameters $a$ and $w_0$ to vary with temperature. Indeed, the thermal expansion of the solid can be conceptualized as a direct consequence of the shifting of the equilibrium separation $w_0$ as a function of temperature, characterized by the familiar linear thermal expansion coefficient $\alpha$ (Shinkai et al., 1981):

$$w_0(T) = w_0^r(1+\alpha\Delta T) \tag{29}$$

where $\Delta T = T - T^r$. On the other hand, it is unclear how the decay length (or the effective range of interaction between two particles) varies with temperature, as there is no direct correlation between $a$ with measurable macroscopic properties of the solid. As a starting point, we adopt a linear relation similar to Eq. (29) as follows (López et al., 2022):

$$a(T) = a^r(1+\beta\Delta T) \tag{30}$$

where the parameter $\beta$ will be discussed together with experimental data in the next section. Substituting Eqs. (29) and (30) in Eqs. (27) and (28) gives the final expressions for $\gamma$ and $K_{IC}$:

$$\frac{\gamma(T)}{\gamma^r} = \frac{E(T)}{E^r}\frac{1}{(1+\alpha\Delta T)(1+\beta\Delta T)^2} \tag{31}$$

$$\frac{K_{IC}(T)}{K_{IC}^r} = \frac{E(T)}{E^r}\sqrt{\frac{1-\nu^{r2}}{1-\nu(T)^2}}\sqrt{\frac{1}{(1+\alpha\Delta T)(1+\beta\Delta T)^2}} \tag{32}$$

### *2.3. Comparing with fracture toughness dataset*

Let us now evaluate the performance of Eq. (32) by comparing it with fracture toughness measurements of solids across various temperatures. Given that this study focuses on the yielding in compression of granular geomaterials like sands and sandstones, this section will accordingly examine $SiO_2$ in crystalline and amorphous forms (i.e., quartz and glass) which have abundant fracture toughness data in the literature.

Meredith and Atkinson (1982) have conducted double torsion (DT) tests on quartz crystals to study the subcritical crack growth (SCG) behavior at various temperatures. Their tests are performed in near vacuum (0.1 - 0.5 Pa) condition, which is important to isolate the effect of humidity and temperature-dependent adsorption on the testing results. To compare the nominal fracture toughness values across different temperatures, the values of stress intensity $K_I$ at a reference crack velocity of $1\times10^{-7}$ m/s are plotted in Figure 3. It is evident that $K_{IC}$ decreases monotonically as the temperature rises from room temperature to 300 °C. For the inputs of Eq. (32), the elastic modulus and Poisson's ratio of quartz at various temperatures reported in Lakshtanov et al. (2007) are adopted, which are summarized in Figure 4. A constant thermal expansion coefficient of $\alpha = 12.01\times10^{-6}/°\text{C}$ for Quartz (Asay et al., 1968) is adopted. The results of Eq. (32) using different $\beta$ values are plotted in Figure 3a. We can see that the model successfully captures the decreasing trend of $K_{IC}$ with temperature, even with a constant decay parameter (i.e., $\beta = 0$). The data is best captured with a $\beta$ value of 0.0015, suggesting that the effective decay length decreases with rising temperature. A similar finding was also reported in a recent experimental study of the structure of heated salt (Zeidler et al., 2022). This calibrated $\beta$ value will be used later in Section 4 for macroscopic modeling of sandstones. We also found that the variation of the equilibrium distance which is represented by the term $(1+\alpha\Delta T)$ has a minimal effect on the prediction given the relatively small value of $\alpha$ for quartz ($\approx 10^{-5}$ /°C)

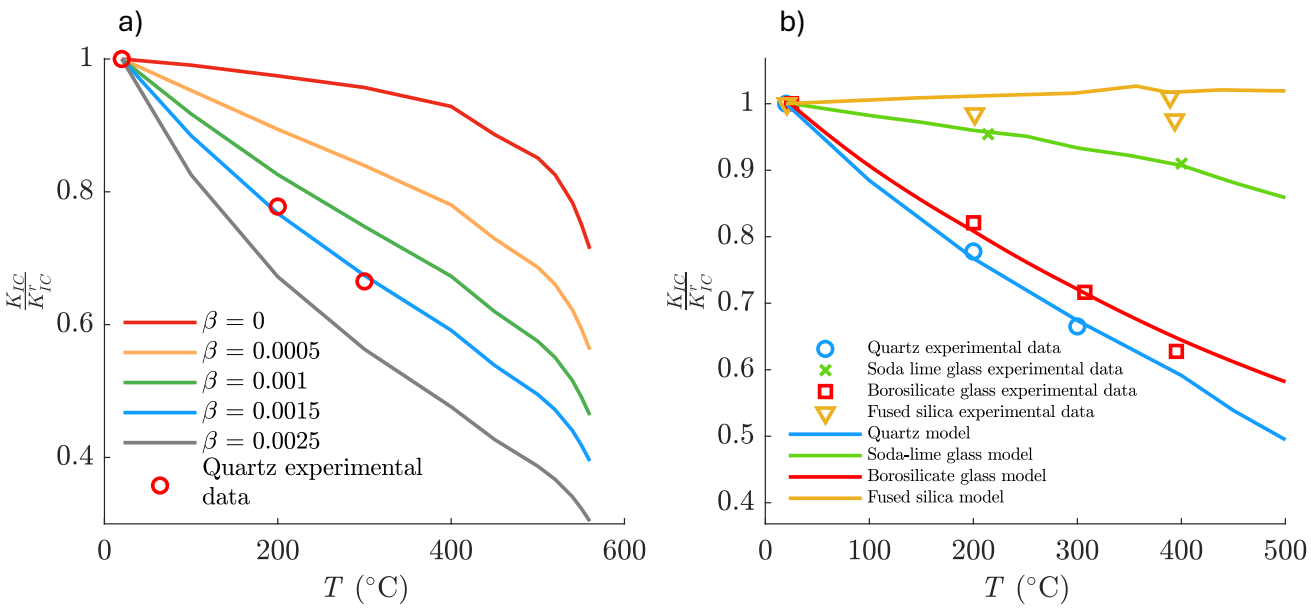


Figure 3: Model (Eq. (32)) vs. experimental data on fracture toughness of a) quartz (Meredith, 1983; Meredith and Atkinson, 1982) and b) fused silica, soda-lime glass, borosilicate glass, and quartz at various temperatures.

In addition, there is an abundance of SCG data for glasses at various temperatures, which could serve as additional benchmarking points to evaluate the model's performance. Figure 3b compiles the $K_{IC}$ of fused silica reported by Wiederhorn et al. (1974), as well as for soda-lime and borosilicate glasses at crack velocity of $1\times10^{-7}$ m/s reported by Wiederhorn et al. (1974), across different temperatures. The results of Eq. (32) using the corresponding $E(T)$, $\nu(T)$, and $\alpha$ data (sources summarized in Table 1), together with the calibrated $\beta$ values are also plotted in the same figure. It is apparent that Eq. (32) or equivalently (31), derived from atomistic arguments and a simple pair potential, proves to be a robust and effective tool for capturing the temperature-dependent $K_{IC}$ and $\gamma$ of brittle solids.

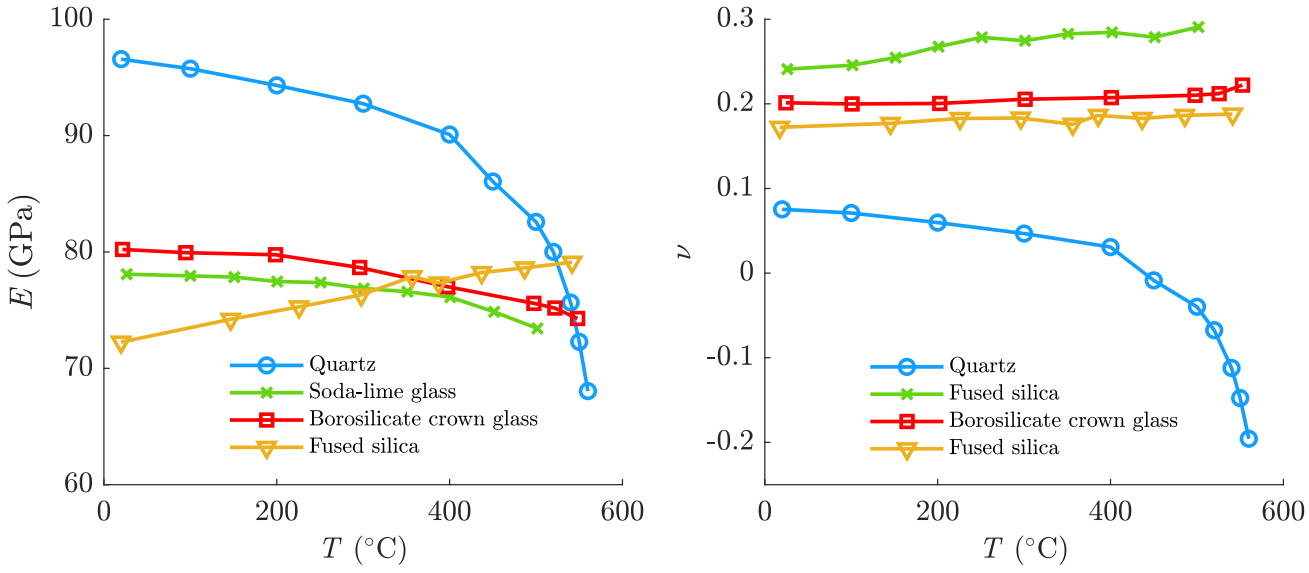


Figure 4: Experimentally measured $E$ and $\nu$ values for silica, soda-lime glass, borosilicate glass, and quartz as functions of temperature. Sources are listed in Table 1.

Table 1: Sources of the values of Young's modulus, Poisson's ratio, and the thermal expansion coefficient, and the calibrated $\beta$ for different materials.

| Material | $E(T)$ | $\nu(T)$ | $\alpha$ [1/°C] | $\beta$ [1/°C] |
|---|---|---|---|---|
| Quartz | (Lakshtanov et al., 2007) | (Lakshtanov et al., 2007) | $12.01\times10^{-6}$ at 20 °C (Asay et al., 1968) | $1.5\times10^{-3}$ |
| Soda-lime glass | (Shinkai et al., 1981) | (Shinkai et al., 1981) | $9\times10^{-6}$ (Shinkai et al., 1981) | $2.3\times10^{-4}$ |
| Borosilicate glass | (Spinner, 1956) | (Spinner, 1956) | $8.68\times10^{-6}$ at ~63 °C (Shartsis and Spinner, 1951) | $1.3\times10^{-3}$ |
| Fused silica | (Pabst and Gregorová, 2013) | (Pabst and Gregorová, 2013) | $5.5\times10^{-7}$ (Shinkai et al., 1981) | $1.5\times10^{-4}$ |

## 3. Surface-based Breakage Mechanics

### *3.1. Thermodynamics of grain crushing*

By applying the thermodynamic analysis outlined in Section 2.1 to a representative elementary volume (REV) of three-dimensional (3D) granular assembly under the same controls, it is possible to show that

the free energy imbalance of the solid skeleton under small-strain condition takes the following form (Zhang, 2018; Zhang and Buscarnera, 2018):

$$\boldsymbol{\sigma}:\dot{\boldsymbol{\varepsilon}}+P\dot{\phi}-\gamma\dot{A}_s-S\dot{T}-\dot{\Psi}^s=\Phi^s\geq 0 \tag{33}$$

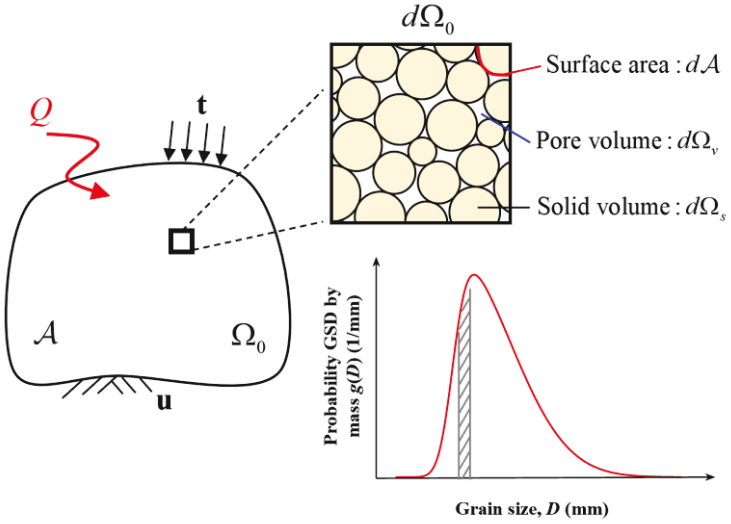


Figure 5: Schematic of a granular system.

where $\boldsymbol{\sigma}$ and $\boldsymbol{\varepsilon}$ are the Cauchy stress and infinitesimal strain tensors, respectively, following the soil mechanics sign convention in which compression is positive and extension is negative; $P$ is the pore fluid pressure; $\phi \equiv d\Omega_v / d\Omega_0 = 1 - d\Omega_s / d\Omega_0$ is the Lagrangian porosity of the solid skeleton, where $d\Omega_v$ is the current pore volume, $d\Omega_s$ the current solid volume, and $d\Omega_0$ the reference total volume of the REV; $A_s \equiv d\mathcal{A} / d\Omega_0$ is the Lagrangian specific surface area where $d\mathcal{A}$ is the amount of solid-fluid interface in the REV. Since the derivation here focuses on an REV, we should clarify that several notations used in Section 2.1 such as the free energy $\Psi$, dissipation rate $\Phi$, entropy $S$, are all normalized by $d\Omega_0$ (per unit reference volume) and are thus volume-specific quantities. If the compressibility of the solid mineral is negligible, porosity change can be equated to volumetric strain through $\dot{\phi} = -\mathrm{tr}(\dot{\boldsymbol{\varepsilon}})$ and Eq. (33) reduces to:

$$\boldsymbol{\sigma}' : \dot{\boldsymbol{\varepsilon}} - \gamma \dot{A}_s - S\dot{T} - \dot{\Psi}^s = \Phi^s \geq 0 \tag{34}$$

where $\boldsymbol{\sigma}' = \boldsymbol{\sigma} - P\mathbf{I}$ is Terzaghi's effective stress. Observing Eq. (34) and considering the inelastic nature of granular materials, we propose that the solid Helmholtz free energy depends on elastic strain, specific surface area, and temperature:

$$\Psi^s = \Psi^s \left( A_s, \boldsymbol{\varepsilon}^e, T \right) \tag{35}$$

where the total strain is decomposed into elastic and plastic strains, i.e., $\boldsymbol{\varepsilon} = \boldsymbol{\varepsilon}^e + \boldsymbol{\varepsilon}^p$. Substituting Eq. (35) into Eq. (34) gives:

$$\left( \boldsymbol{\sigma}' - \frac{\partial \Psi_s}{\partial \boldsymbol{\varepsilon}^e} \right) : \dot{\boldsymbol{\varepsilon}}^e + \left( -S - \frac{\partial \Psi^s}{\partial T} \right) \dot{T} + \left( -\gamma - \frac{\partial \Psi^s}{\partial A_s} \right) \dot{A}_s + \boldsymbol{\sigma}' : \dot{\boldsymbol{\varepsilon}}^p = \Phi^s \geq 0 \tag{36}$$

It is worth noting that $A_s$ is an observable but not a controllable quantity for a granular system. Therefore $A_s$ is not an external state variable like $\boldsymbol{\sigma}'$ or $T$ but should be taken as an internal state variable (ISV) similar to plastic strain $\boldsymbol{\varepsilon}^p$. For reversible processes (i.e., $\Phi^s = 0$, $\dot{\boldsymbol{\varepsilon}}^p = 0$, and $\dot{A}_s = 0$), the elastic constitutive relations are obtained:

$$\boldsymbol{\sigma}' = \frac{\partial \Psi^s}{\partial \boldsymbol{\varepsilon}^e} \; ; \; S = -\frac{\partial \Psi^s}{\partial T} \tag{37}$$

For irreversible processes, substitute Eq. (37) into Eq. (36) gives the thermodynamic constraint for the system's evolution:

$$\left( E_s - \gamma \right) \dot{A}_s + \boldsymbol{\sigma}' : \dot{\boldsymbol{\varepsilon}}^p = \Phi^s \left( \dot{A}_s, \dot{\boldsymbol{\varepsilon}}^p \right) \geq 0 \tag{38}$$

where $E_s \equiv -\partial \Psi^s / \partial A_s$ is analogous to $G$ in fracture mechanics, characterizing the elastic energy release rate due to surface area growth in the REV. Eq. (38) shows that energy dissipation in brittle granular

materials can be caused by the growth of surface area through cracking and grain breakage, as well as plastic deformation associated with friction and grain rearrangement (Nguyen and Einav, 2009). Without plasticity, Eq. (38) reduces to:

$$\left(E_s-\gamma\right)\dot{A}_s \geq 0 \tag{39}$$

which can be viewed as the analogue of Rice's criterion (14) for a material REV with evolving internal surface area.

Eq. (38) may be rearranged into

$$E_s\dot{A}_s+\boldsymbol{\sigma}':\dot{\boldsymbol{\varepsilon}}^p=\Phi^s\left(\dot{A}_s,\dot{\boldsymbol{\varepsilon}}^p\right)+\gamma\dot{A}_s\equiv\Phi^*\left(\dot{A}_s,\dot{\boldsymbol{\varepsilon}}^p\right)\geq 0 \tag{40}$$

In writing Eq. (40), we have taken an alternative view to the crushing energetics: the energy budget required to overcome the surface energy $\gamma\dot{A}_s$ is now considered as part of a lumped dissipation rate $\Phi^*$, rather than as an energy transfer from the solid to the surface phase. Mathematically, this grants greater flexibility in defining the inelastic evolution laws of the system, as the lumped dissipation $\Phi^*$ is not constrained to take an additive form $\left(\Phi^s+\gamma\dot{A}_s\right)$ but may take other coupled forms. This choice is also physically justified. Studies have shown that a breakage event in a granular matrix immediately triggers a sequence of grain rearrangements, the energy dissipated through which are often inseparable from each other (Einav, 2007b; Russell and Einav, 2013)

Complete constitutive relations can be established once the expressions of the free energy $\Psi^s\left(A_s,\boldsymbol{\varepsilon}^e,T\right)$ and the dissipation rate $\Phi^*\left(\dot{A}_s,\dot{\boldsymbol{\varepsilon}}^p\right)$ are specified, together with the adoption of orthogonality principle (Houlsby and Puzrin, 2007; Ziegler, 1977). We now shift our focus to constructing these expressions based on sound micromechanical arguments and experimental observations.

351

352 ***3.2. Surface area – GSD relation***

353 The free energy of the crushable granular materials takes a multiplicative form of (Einav, 2007a, b):

354 $$\Psi^s = \hat{f}\psi_r\left(\boldsymbol{\varepsilon}^e, T\right) \tag{41}$$

355 where $\psi_r$ is the reference Helmholtz free energy; pre-factor $\hat{f}$ characterizes how the free energy scales
356 with the grain size distribution of the assembly. In the original CBM theory, analyzing the energy split
357 among different grain size fractions and performing statistical homogenization with respect to GSD gives
358 an expression of the pre-factor $\hat{f} = 1 - \vartheta B$, where $B$ is the *breakage* internal state variable that traces the
359 current GSD and $\vartheta$ is a grading index dependent on the initial and ultimate GSDs. To inherent this
360 appealing micromechanical basis, while keeping the benefit having $A_s$ and $\gamma$ in the model formulation,
361 it is desirable to seek a relation between $A_s$ and the GSD of the granular assembly, through which the pre-
362 factor $\hat{f}$ can be expressed in terms of $A_s$.

363 Observing Figure 5 and considering solid incompressibility, the total volume of solid grains $d\Omega_s$ is given
364 by:

365 $$d\Omega_s = \left(J - \phi\right) d\Omega_0 = \left(1 - \phi_0\right) d\Omega_0 \tag{42}$$

366 where $J = d\Omega_t / d\Omega_0$ is the Jacobian; $d\Omega_t$ is the current total volume of the REV. Let $g(D)$ be the
367 probability GSD by mass, the volume of grains $d\Omega_s^D$ within size range $\left(D, D + dD\right)$ is therefore,

368 $$d\Omega_s^D = \left(1 - \phi_0\right) g\left(D\right) d\Omega_0 dD \tag{43}$$

Dividing Eq. (43) by the volume of each grain $\beta_V D^3$ gives the number of grains $N_D$ with size $(D, D+dD)$:

$$N_D = \frac{(1-\phi_0)\, g(D)\, d\Omega_0 dD}{\beta_V D^3} \tag{44}$$

The specific surface area of the REV can be readily calculated by:

$$A_s = \frac{d \triangleq}{d\Omega_0} = \frac{d}{d\Omega_0} \int_{D_m}^{D_M} \left(\beta_A D^2\right) N_D dD = \frac{(1-\phi_0)\beta_A}{\beta_V} \left\langle D^{-1} \right\rangle \tag{45}$$

where $\left\langle D^k \right\rangle = \int_{D_m}^{D_M} g(D) D^k dD$ is the $k$th order moment of the grain size distribution $g(D)$; $\beta_A$ and $\beta_V$ are shape factors relating grain size to the surface area and volume of the grain, respectively (e.g., $\beta_A = \pi$ and $\beta_V = \pi/6$ for spherical particles); $D_m$ and $D_M$ are minimum and maximum grain sizes, respectively.

Eq. (45) connects the specific surface area $A_s$ with the current GSD through $\left\langle D^{-1} \right\rangle$. In addition, it also hints a dependency of grain shape as the shape factors $\beta_A$ and $\beta_V$ can evolve during the course of breakage. Buscarnera and Einav (2021) recently provided a thorough treatise on the effect of co-evolving grain size and shape in the crushing dynamics of granular materials. Here, we make the simplifying assumption that these factors do not evolve throughout the course of crushing.

It is worth noting that Eq. (45) provides a one-way mapping from GSD to $A_s$. However, a given $A_s$ can correspond to infinitely many GSDs. To further constrain the $A_s$-GSD relation, one must specify the form of the GSD and prescribe its relation to the initial and ultimate states. A simple equation that represent the initial and ultimate gradations is given by (Einav, 2007a; Zhang and Buscarnera, 2014):

$$g_0(D)=\frac{(3-\chi_0)D^{2-\chi_0}}{D_M{}^{3-\chi_0}-D_m{}^{3-\chi_0}}\ ;\ g_u(D)=\frac{(3-\chi_u)D^{2-\chi_u}}{D_M{}^{3-\chi_u}-D_m{}^{3-\chi_u}} \tag{46}$$

where $\chi_0$ and $\chi_u$ are initial and ultimate fractal dimensions, respectively. An initially poorly-graded GSD can be represented by setting a low $\chi_0$ value, and the ultimate GSD typically has $\chi_u = 2.5 \sim 2.6$ (Sammis et al., 1987). In the original CBM (Einav, 2007a), the current GSD is determined by linearly interpolating between the initial and the ultimate GSDs using a breakage variable *B*:

$$g(D,B)=(1-B)g_0(D)+Bg_u(D) \tag{47}$$

Eq. (47) essentially parametrized the evolution of a probability distribution function by a scalar ISV, *B*, which significantly facilitated the engineering applications of breakage mechanics (Zhang et al., 2013; Zhou et al., 2019). However, the linear relation between the current GSD and the two end members can sometimes overpredict the amount of fines generated during crushing − an important factor in accurately predicting the hydraulic properties of granular materials (Gao et al., 2016; Singh et al., 2021).

Given that the current model (41) utilizes $A_s$ instead of *B* to track the crushing process within the REV, we have the flexibility to redefine how the GSD evolves relative to the two end members. Close examination of experimental data and discrete element method (DEM) simulation results shows that the fractal dimension, especially among smaller grain size fractions, gradually increases throughout the collective crushing process (Ben-Nun and Einav, 2010; Cheng and Wang, 2021; Lobo-Guerrero et al., 2006; Wang et al., 2019). This motivated us to propose directly taking the fractal dimension $\chi$ as an evolving variable that traces the GSD evolution

$$g(D,\chi)=\frac{(3-\chi)D^{2-\chi}}{D_M{}^{3-\chi}-D_m{}^{3-\chi}} \tag{48}$$

405 , in replace of the linear relation Eq. (47). Figure 6a and b compares the GSDs in terms of the number of
406 particles $N(>D)$ vs. the grain size $D$ calculated from Eq. (47) and Eq. (48), respectively. We can see
407 that Eq. (48) depicts a gradual increase in the $N$ vs. $D$ slope, while (47) predicts the slope within fine
408 particles reaching ultimate value $\chi_u$ at the very beginning of collective crushing.

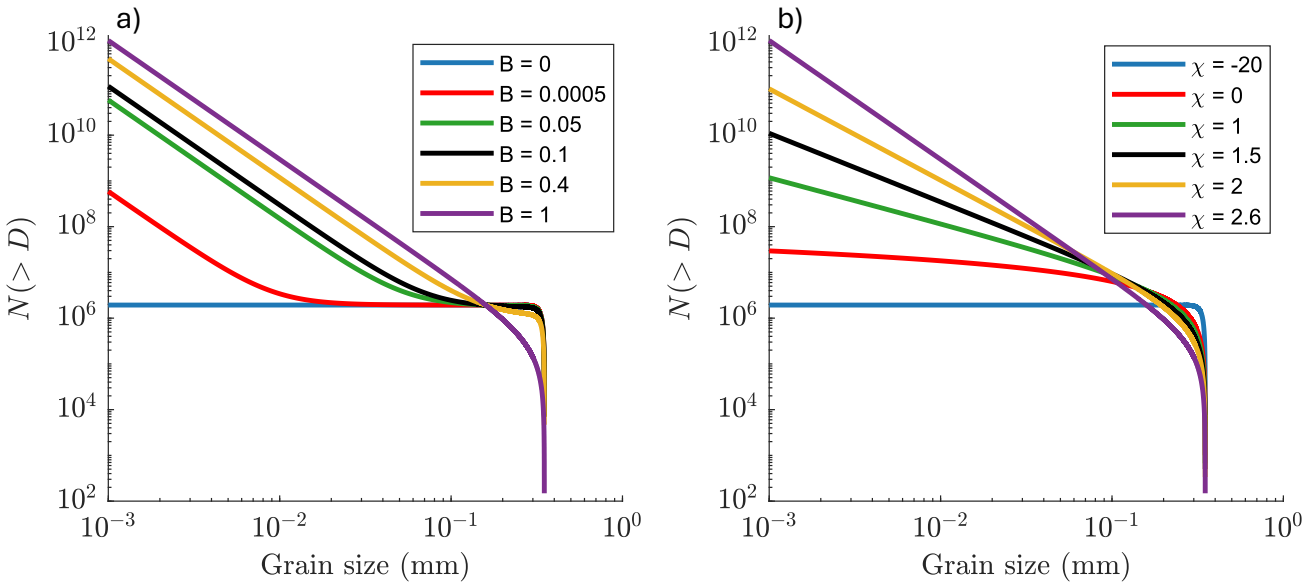

409

410 Figure 6: Number of particles $N(>D)$ vs the grain size $D$ at a) different breakage values using Eq. (47);
411 b) different fractal dimensions using Eq. (48). Parameters used for the initial and ultimate GSDs:
412 $\chi_0 = -20$, $\chi_u = 2.6$, $D_m$= 0.001 mm, $D_M$=0.35 mm. $N$ is calculated based on 100 grams of spherical
413 grains with intrinsic density of 2650 kg/m$^3$.

414 Figure 7 reports the GSDs of carbonate sand obtained through X-ray CT images at different axial strains
415 during a triaxial compression test with confining pressure = 1900 kPa (Cheng and Wang, 2021). Eqs. (47)
416 and (48) are calibrated to best capture the GSDs and presented in the same plot. We can see that the slope
417 of the $N(>D)$ vs. $D$ lines, in the region from 0.1 mm to 0.3 mm, increases gradually as the sample
418 undergoes shearing, which is only captured through the fractal-based GSD Eq. (48). Figure 8 presents the
419 second dataset from zeolite granules subjected to oedometric compression (Wang et al., 2019), along with
420 the fitted curves from the two equations. Eq. (48) again offers a better fit to the GSD data across most

grain size ranges and strain levels. The resulting $A_s$ – GSD relation follows by combining Eqs. (45) and (48):

$$A_s(\chi) = \frac{(1-\phi_0)\beta_A}{\beta_V} \frac{(3-\chi)}{(2-\chi)} \frac{\left(D_M{}^{2-\chi} - D_m{}^{2-\chi}\right)}{\left(D_M{}^{3-\chi} - D_m{}^{3-\chi}\right)} \tag{49}$$

Eq. (49) describes the evolution of the specific surface area with the evolution of the GSD via the fractal dimension $\chi$ while assuming the shape factors $\beta_A$ and $\beta_V$ remains constant throughout the course of loading and considering solid incompressibility.

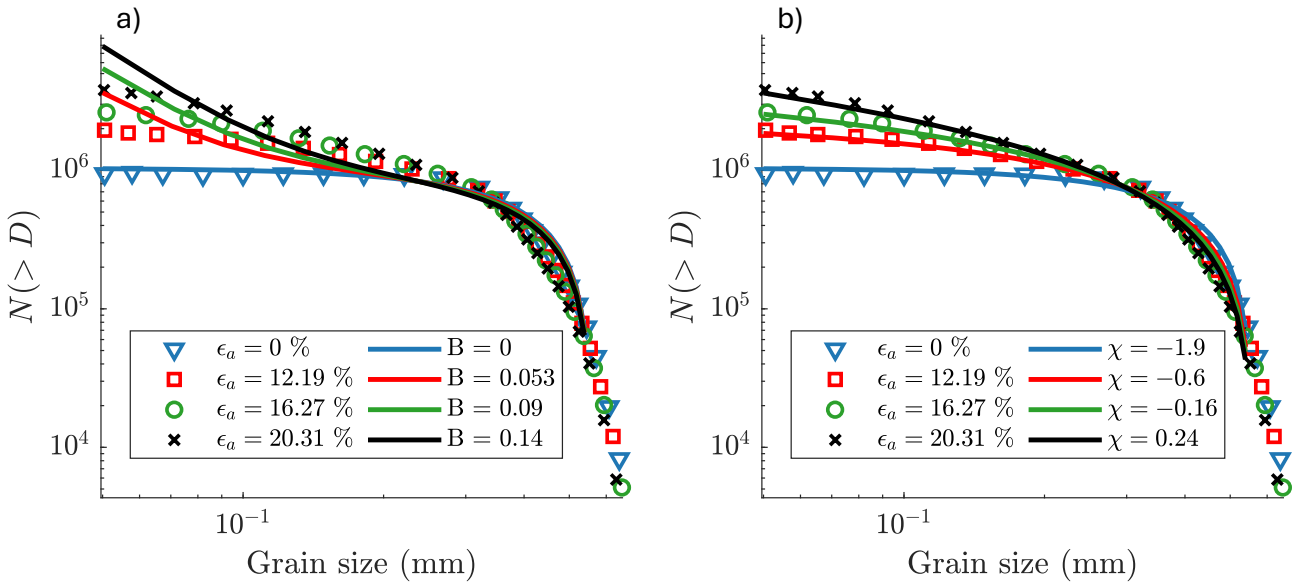


Figure 7: Comparison of a) Eq. (47) and b) Eq. (48) with the GSD data of carbonate sand subjected to triaxial compression from Cheng and Wang (2021). For the models, total mass was set to 100 grams, and the density of the carbonate sand is 2710 Kg/m$^3$ (Fadia et al., 2021). Both a) and b) have the same fractal initial and ultimate GSDs with a fractal dimension of -1.9 and 2.6, respectively. The minimum and maximum grain sizes for the initial and ultimate GSDs are 0.05 mm and 0.56 mm, respectively.

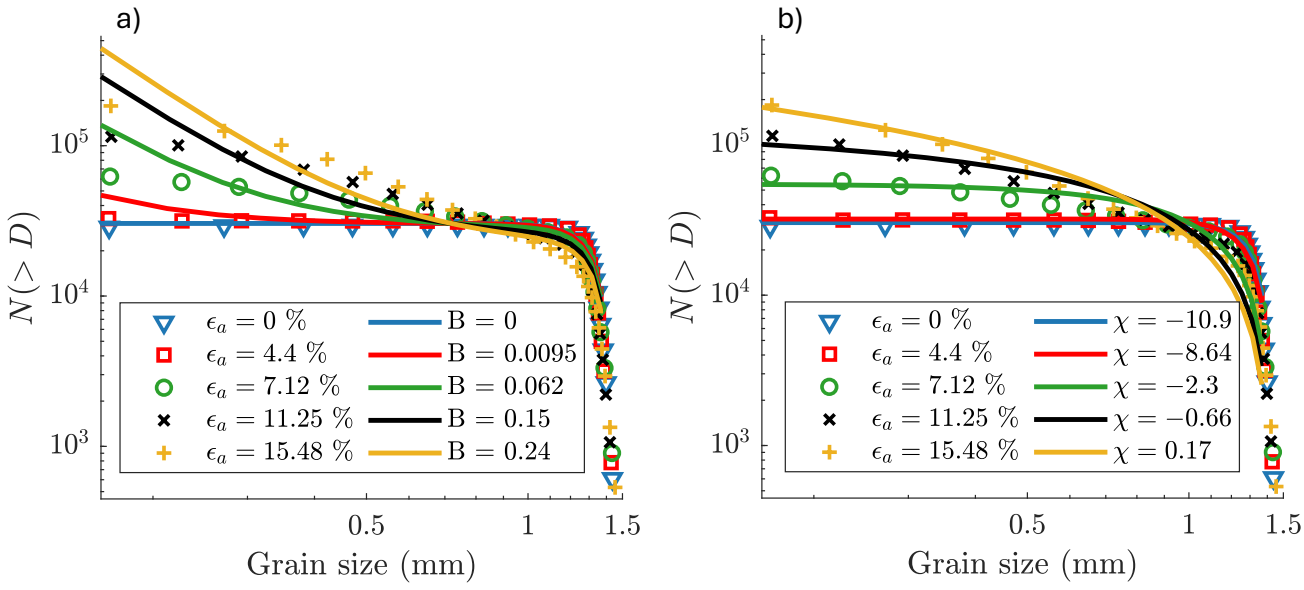


Figure 8: Comparison of a) Eq. (47) and b) Eq. (48) with the GSD data of zeolite granules under oedometric compression from Wang et al. (2019). Total mass was set to 100 grams, and the density of the zeolite granules is 2810 Kg/m$^3$. Both a) and b) have the same fractal initial and ultimate GSDs with a fractal dimension of -10.9 and 2.6, respectively. The minimum and maximum grain sizes for the initial and ultimate GSDs are 0.16 and 1.42 mm, respectively.

### *3.3. Helmholtz free energy*

The Helmholtz free energy for a polydisperse granular assembly can be constructed by (Einav, 2007a):

$$\Psi^s = \Psi^s\left(\boldsymbol{\varepsilon}, A_s(\chi), T\right) = \int_{D_m}^{D_M} \hat{\psi}\left(\boldsymbol{\varepsilon}, D, T\right) g\left(D, \chi\right) dD \tag{50}$$

where $\hat{\psi}$ is the specific Helmholtz free energy stored in grain size fraction $\left(D, D+dD\right)$:

$$\hat{\psi}(D, \boldsymbol{\varepsilon}, T) = \left(\frac{D}{D_r}\right)^n \psi_r(\boldsymbol{\varepsilon}, T) \tag{51}$$

where $D_r$ is a reference grain size. By hypothesizing that the elastic energy stored in each grain size fraction is proportional to the surface area of the grains, it is possible to set $n = 1$ for a system of disk-

shaped particles and $n=2$ for spherical particles (Einav, 2007a). Substituting Eq. (51) in Eq. (50) gives the multiplicative expression Eq. (41) with a new expression for the pre-factor $\hat{f}\left(A_s\left(\chi\right)\right)$:

$$\hat{f}\left(A_s\left(\chi\right)\right)=\frac{\left(3-\chi\right)}{\left(n+3-\chi\right)}\frac{\left(D_M^{n+3-\chi}-D_m^{n+3-\chi}\right)}{\left(D_M{}^{3-\chi}-D_m{}^{3-\chi}\right)}D_r{}^{-n} \tag{52}$$

We choose the reference grain size $D_r$ such that $\hat{f}=1$ at $\chi=\chi_0$. This gives:

$$D_r=\left[\frac{\left(D_M{}^{3-\chi_0}-D_m{}^{3-\chi_0}\right)\left(n+3-\chi_0\right)}{\left(D_M{}^{n+3-\chi_0}-D_m{}^{n+3-\chi_0}\right)\left(3-\chi_0\right)}\right]^{-\frac{1}{n}} \tag{53}$$

Substituting (53) into (52) and setting $n=2$ gives the final expression for $\hat{f}$:

$$\hat{f}\left(A_s\left(\chi\right)\right)=\frac{\left(5-\chi_0\right)}{\left(3-\chi_0\right)}\frac{\left(3-\chi\right)}{\left(5-\chi\right)}\frac{\left(D_M{}^{3-\chi_0}-D_m{}^{3-\chi_0}\right)}{\left(D_M{}^{5-\chi_0}-D_m{}^{5-\chi_0}\right)}\frac{\left(D_M{}^{5-\chi}-D_m{}^{5-\chi}\right)}{\left(D_M{}^{3-\chi}-D_m{}^{3-\chi}\right)} \tag{54}$$

For simplicity, the reference Helmholtz free energy is chosen such that it would produce linear thermoelastic relations (Kokash et al., 2024)

$$\psi_r(\varepsilon_v^e,\varepsilon_s^e,T)=\frac{1}{2}K_g\left[\varepsilon_v^e-3a\left(T-T_0\right)\right]^2+\frac{3}{2}G_g\varepsilon_s^{e2}-\frac{C}{T_0}\frac{(T-T_0)^2}{2} \tag{55}$$

where $K_g$ and $G_g$ are the bulk and the shear modulus of the granular assembly, respectively; $\varepsilon_v=\mathrm{tr}(\boldsymbol{\varepsilon})$ and $\varepsilon_s=\sqrt{2e_{ij}e_{ij}/3}$ are the volumetric and deviatoric strains, respectively; $e_{ij}=\varepsilon_{ij}-\frac{\varepsilon_{kk}}{3}\delta_{ij}$ is the strain deviator; $T_0$ is a reference temperature; $a$ is the thermal expansion coefficient of the overall REV; $C$ is the heat capacity of the REV. Substituting Eq. (55) in Eq. (41) gives the elastic relations:

461
$$\begin{cases} p' = \dfrac{\partial \Psi^s}{\partial \varepsilon_v^e} = \hat{f}\, K_g \left[ \varepsilon_v^e - 3a\left(T - T_0\right) \right] \\ q = \dfrac{\partial \Psi^s}{\partial \varepsilon_s^e} = 3\hat{f}\, G_g \varepsilon_s^e \\ S = -\dfrac{\partial \Psi^s}{\partial T} = C\left( \dfrac{T}{T_0} - 1 \right) \\ E_s = -\dfrac{\partial \Psi^s}{\partial A_s} = -\dfrac{\partial \hat{f}}{\partial \chi}\dfrac{\partial \chi}{\partial A_s}\left\{ \dfrac{1}{2} K_g \left[ \varepsilon_v^e - \varepsilon_v^{th} \right]^2 + \dfrac{3}{2} G_g \varepsilon_s^{e2} \right\} \end{cases} \tag{56}$$

462 where $p' = (1/3)\sigma_{ii}$ and $q = \sqrt{3 s_{ij} s_{ij} / 2}$ are the mean effective stress and the deviatoric stress,
463 respectively; $s_{ij} = \sigma_{ij} - p'\delta_{ij}$ the stress deviator. The derivatives $\partial \hat{f} / \partial \chi$ and $\partial \chi / \partial A_s$ in Eq. (56) can be
464 obtained via Eqs. (49) and (52), respectively. It is worth noting that the elastic constants $K_g$ and $G_g$ may
465 be functions of temperature as well, which will have implications on the overall yielding through the
466 energy release rate $E_s$. This aspect will be discussed in detail together with experimental data in Section
467 4.

468 ***3.4. Dissipation rate, flow rules, and yield surface***

469 Total dissipation comprises contributions from plastic deformation and surface-area growth. Since these
470 mechanisms are generally coupled and inseparable, the combined dissipation can be expressed as (Einav,
471 2007b):

472
$$\Phi^*\left( \dot{\varepsilon}_v^p, \dot{\varepsilon}_s^p, \dot{A}_s \right) = \sqrt{\left( \Phi_{pv}\left( \dot{\varepsilon}_v^p \right) \right)^2 + \left( \Phi_{ps}\left( \dot{\varepsilon}_s^p \right) \right)^2 + \left( \Phi_A\left( \dot{A}_s \right) \right)^2} \tag{57}$$

473 where $\Phi_{pv}$, $\Phi_{ps}$, and $\Phi_A$ are the plastic volumetric, plastic shear, and surface growth dissipation rates,
474 respectively. They are proposed to take the following forms:

$$\Phi_{pv} = \sqrt{\frac{\gamma H}{E_s}} \frac{p'}{\sin(\omega)} \dot{\varepsilon}_v^p$$

$$\Phi_{ps} = (Mp' + c)\dot{\varepsilon}_s^p \tag{58}$$

$$\Phi_A = \frac{\sqrt{E_s \gamma H}}{\cos(\omega)} \dot{A}_s$$

where $M$ is a critical state parameter that defines the ratio between the shear and mean stresses when the material is sheared up to steady state; $c$ is cohesion; $\omega$ is coupling parameter controls the contribution of surface growth dissipation in the post-yield stage; $H = H(A_s)$ governs the hardening behavior by scaling the energy budget for grain crushing as a function of specific surface area. Since crushable granular materials usually display clastic hardening following initial yield, $H$ increases monotonically with $A_s$:

$$H(A_s) = R\left(\frac{A_{su} - A_{s0}}{A_{su} - A_s}\right)^s \tag{59}$$

where $A_{s0}$ and $A_{su}$ are the specific surface areas at initial and ultimate state which can be calculated from Eq. (49) by setting $\chi = \chi_0$ and $\chi = \chi_u$, respectively; parameter $s$ controls the rate of hardening; $R$ is an augmentation parameter that characterizes the extra energy dissipation associated with the rearrangement of the grains (McDowell and Bolton, 1998; Russell, 2011; Russell and Einav, 2013). In other words, $R$ amplifies the energy required to initiate grain crushing to account for the fact that, when a particle break, energy is not only spent to create new surface areas, but also to accommodate load redistribution and particle rearrangements within the granular assembly (Russell, 2011). It will be further elaborated in Section 5.1, along with its calibrated values.

Noting that $\Phi^*$ defined in Eqs. (57) and (58) is a first-order homogenous function of the inelastic rates, we can write

$$\Phi^* = \overset{\bar{p}'}{\frac{\partial \Phi^*}{\partial \dot{\varepsilon}_v^p}} \dot{\varepsilon}_v^p + \overset{\bar{q}}{\frac{\partial \Phi^*}{\partial \dot{\varepsilon}_s^p}} \dot{\varepsilon}_s^p + \overset{\bar{E}_s}{\frac{\partial \Phi^*}{\partial \dot{A}_s}} \dot{A}_s \tag{60}$$

where stresses with the overhead bar $\left(\bar{p}', \bar{q}, \bar{E}_s\right)$ denotes dissipative stresses conjugate to the inelastic rates $\left(\dot{\varepsilon}_v^p, \dot{\varepsilon}_s^p, \dot{A}_s\right)$. Performing Legendre transform on $\Phi^*$ and observing Eq. (60) gives (Houlsby and Puzrin, 2007):

$$\bar{w}\left(\bar{p}', \bar{q}, \bar{E}_s\right) = \lambda \bar{y}\left(\bar{p}', \bar{q}, \bar{E}_s\right) = \bar{p}' \dot{\varepsilon}_v^p + \bar{q} \dot{\varepsilon}_s^p + \bar{E}_s \dot{A}_s - \Phi^*\left(\dot{\varepsilon}_v^p, \dot{\varepsilon}_s^p, \dot{A}_s\right) = 0 \tag{61}$$

where $\bar{w}$ and $\bar{y} \le 0$ are the flow potential and the yield function in dissipative stress space, respectively; $\lambda \ge 0$ is a plastic multiplier and satisfies the Kuhn-Tucker condition with $\bar{y}$. Substituting Eq. (57) into (61) gives a canonical form of $\bar{y}$:

$$\bar{y} = \left(\frac{\bar{p}'}{\partial \Phi_{pv} / \partial \dot{\varepsilon}_v^p}\right)^2 + \left(\frac{\bar{q}}{\partial \Phi_{ps} / \partial \dot{\varepsilon}_s^p}\right)^2 + \left(\frac{\bar{E}_s}{\partial \Phi_s / \partial \dot{A}_s}\right)^2 - 1 \le 0 \tag{62}$$

The flow rules are given by:

$$\dot{A}_s = \frac{\partial \bar{w}}{\partial \bar{E}_s} = \lambda \frac{\partial \bar{y}}{\partial \bar{E}_s}\ ;\ \dot{\varepsilon}_v^p = \frac{\partial \bar{w}}{\partial \bar{p}'} = \lambda \frac{\partial \bar{y}}{\partial \bar{p}'}\ ;\ \dot{\varepsilon}_s^p = \frac{\partial \bar{w}}{\partial \bar{q}} = \lambda \frac{\partial \bar{y}}{\partial \bar{q}} \tag{63}$$

Substituting Eq. (58) in Eq. (62) and enforcing the normality rule (Ziegler, 1983) in the form of $\bar{p}' = p'$, $\bar{q} = q$, $\bar{E}_s = E_s$ the yield function in true stress space is derived as:

$$y = \frac{E_s}{\gamma H} + \frac{q^2}{\left(Mp' + c\right)^2} - 1 \le 0 \tag{64}$$

One can see that, as a consequence of the coupled energy dissipation assumed in Eq. (57), the onset of yielding in the granular material depends on both surface area growth and frictional dissipation. The first term on the right-hand side captures the competition between the driving energy release rate $E_s$ and the mineral surface energy $\gamma(T)$, modulated by a hardening function. The second term measures the driving shear stress relative to the frictional resistance arising from normal stress and cohesion, consistent with a simple Mohr–Coulomb law.

The flow rules derived from Eqs. (58), (62), and (63) are:

$$\dot{A}_s = \frac{2\lambda \cos^2(\omega)}{\gamma H};\ \dot{\varepsilon}_v^p = \frac{2\lambda E_s \sin^2(\omega)}{p'\gamma H};\ \dot{\varepsilon}_s^p = \frac{2\lambda q}{(Mp'+c)^2} \tag{65}$$

The incremental constitutive relation and a brief description of its implementation in a material-point driver is given in the Appendix.

## 4. Model performance

### *4.1. Thermal weaking of sandstones*

Experimental data from Jefferd et al. (2021) on sandstones have shown that temperature plays an important role in the weaking of sandstones. They have conducted triaxial compressions tests on three sandstones (Bleursville, Locharbriggs, and Boise) under effective confining pressures ranging from 5 to 120 MPa and at two temperatures, 20 °C and 150 °C. The samples were water-saturated before and throughout the tests under a pore pressure of 5 MPa. All three sandstones exhibited similar temperature dependent behavior, show weakening when the temperature was raised to 150 °C. The peak or the cataclastic flow deviatoric stress decreased by 11-30% for Bleursville, 3-20% for Locharbriggs, and 12-33% for Boise sandstones, depending on the confining pressure. The authors posited three thermal weakening mechanisms: intergranular pressure solution, reduced internal friction coefficient and fracture toughness, and

accelerated crack propagation kinetics (subcritical crack growth). After analyzing each factor, they concluded that the primary driver is the reduction in fracture toughness at elevated temperatures. Here, we will test this hypothesis using the proposed surface-based breakage model, for its ability to isolate the surface energy from other factors influencing the stress-strain behavior of granular rocks.

We focus on the Bleursville and Locharbriggs sandstones, whose predominantly quartz composition enables a direct comparison with our single-crack-scale surface-energy study on quartz. The initial porosity, and constituents of each of the sandstone are presented in Table 2 (Jefferd et al., 2021). The reported GSDs of Bleursville sandstone by Ashari et al. (2017) and that of Locharbriggs sandstone by Baraka-Lokmane et al. (2009) are used to determine the maximum grain size $D_M$ and the initial fractal dimension $\chi_0$, as shown in Figure 9 and Table 3. For the minimum grain size, we choose a fixed value of 1 $\mu$m for the two sandstones. The ultimate fractal dimension $\chi_u$ is set to 2.6.

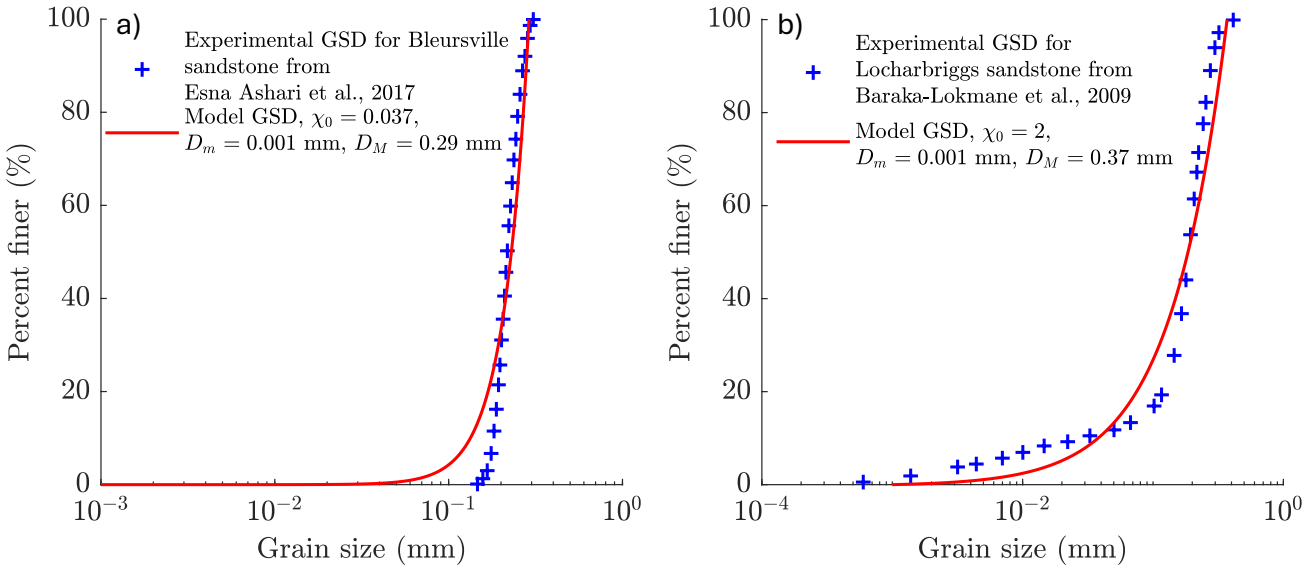


Figure 9: Experimental GSD for a) Bleursville sandstone and b) Locharbriggs sandstone along with fractal GSD fitting.

Table 2: Porosity and Constituents for Bleursville sandstone, Locharbriggs sandstone, and St. Peter quartz sand (Carr, 1971; Jefferd et al., 2021).

| Sandstone | Initial porosity | Constituents |
|---|---|---|
| Bleursville sandstone | 22.7% | Quartz (66%), K-feldspar (28%), clays (4%), and mica (2%) |
| Locharbriggs sandstone | 24.3% | Quartz (88%) and K-Feldspar (6%) |
| St. Peter quartz Sand | 32.4 % | Quartz (99.4%), oxides (0.6%) |

Table 3: Parameters used for Bleursville sandstone, Locharbriggs sandstone, and St. Peter quartz sand.

| Material | Mechanical parameters | | | | | | | | GSD parameters | | | |
|---|---|---|---|---|---|---|---|---|---|---|---|---|
| | $K_g$ MPa | $G_g$ MPa | $\gamma$ J/m$^2$ | $M$ - | $c$ MPa | $\omega$ $^o$ | $s$ - | $R$ - | $\chi_0$ - | $\chi_u$ - | $D_m$ mm | $D_M$ mm |
| Bleursville sandstone | 5000 | 2750 | 6 | 1.21 | 24 | 79 | 6 | 18.92 | 0.037 | 2.6 | $1\times10^{-3}$ | 0.29 |
| Locharbriggs sandstone | 5800 | 3750 | 6 | 1.52 | 23 | 85 | 2.6 | 3 | 2 | 2.6 | $1\times10^{-3}$ | 0.37 |
| St. Peter quartz Sand | 1330 | 860 | 6 | 1.13 | 0 | 65 | 2 | 57.5 | -1.94 | 2.6 | $1\times10^{-3}$ | 0.35 |

The mechanical parameters of the model are calibrated with experimental data at 20 °C and are reported in Table 3. Since all tests are conducted at isothermal condition $T = T_0$ (albeit at different temperatures), the incremental constitutive relation contains neither $a$ nor $C$, therefore their values are not needed. The reference surface energy for quartz ranges from 0.28 to 11.5 J/m$^2$ (Parks, 1984), we will choose an average value of 6 J/m$^2$. Note that, theoretically, all parameters ($K_g$, $G_g$, $M$, etc.) can be temperature dependent. However, to test the hypothesis that thermal weakening of sandstones, in the temperature range of 20 °C and 150 °C, is primarily driven by a reduction in surface energy, we deliberately hold all other parameters constant and allow only $\gamma$ to vary with temperature, as governed by Eq. (31). Fine tuning is not permitted because all parameters for quartz have been already determined in Figure 3 (a).

Figure 10 (a) and (b) show the deviatoric stress ($q$) vs. the axial strain ($\varepsilon_a$) data for Bleursville and Locharbriggs sandstones at 100 MPa confining pressure at 20 and 150 °C as well as the model predictions using parameters listed in Table 3. It is observed that the model accurately captured the temperature-dependent yielding points of both sandstone samples and provided a good overall match to the stress–strain curves. Considering the yield function Eq. (64) involves the elastic energy release rate $E_s$ which further depends on elastic properties via Eq. (56), one may suspect that the apparent thermal dependence of yielding could be due to temperature effects on $K_g$ and $G_g$. However, as shown in Figure 10, the experimental data in the pre-yielding regime exhibit minimal variations in slope, supporting the use of constant $K_g$ and $G_g$ values over the temperature range of interest. This agreement between the model and the data corroborates that the thermal weakening of the tested sandstones below 150 °C arises primarily from a decrease in the surface energy of the constituent minerals.

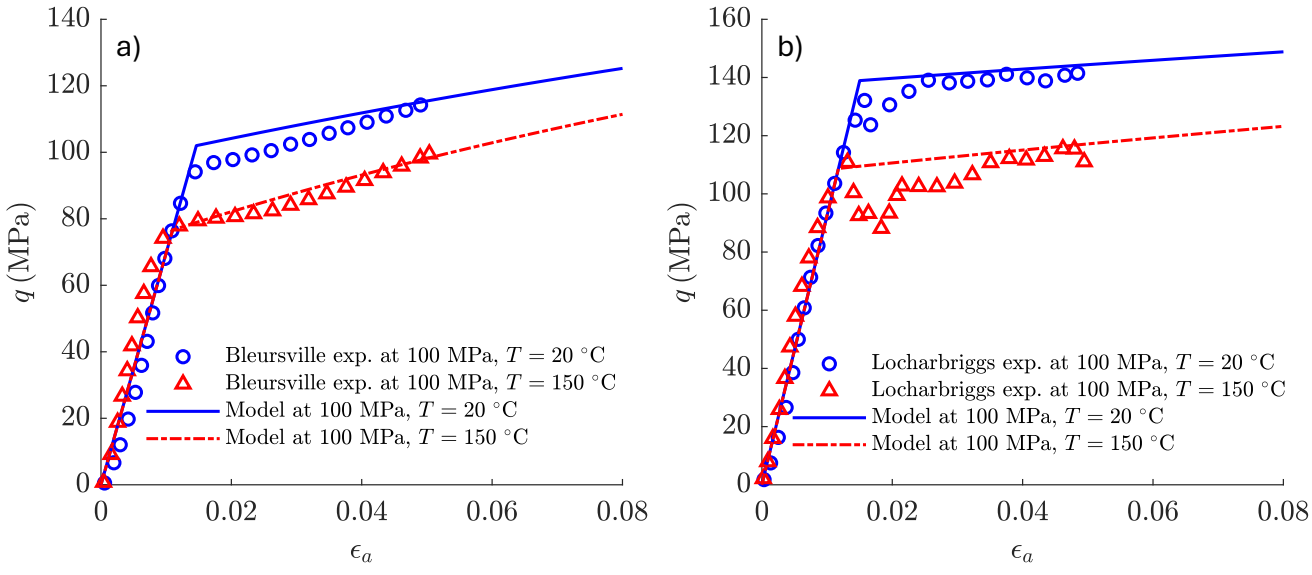


Figure 10: Deviatoric stress ($q$) vs axial strain ($\varepsilon_a$) for a) Bleursville sandstone and b) Locharbriggs sandstone at 100 MPa confining pressure at 20 and 150 °C.

A more comprehensive view of the temperature-dependent yielding across different confining pressures can be visualized by plotting the yield surface in the $p'$ vs. $q$ plane (Figure 11). The experimental yield points in Figure 11 are the peak or cataclastic flow stresses reported in Jefferd et al. (2021). One can see a clear shrinkage of the yield surface as temperature elevates. The yield pressure ( $p'^*$ ) during isotropic compression, which is also called clastic yielding and is governed by the onset of grain crushing, can be analytically calculated in the present model. Substituting Eq. (56) in Eq. (64) and setting $q = 0$ gives:

$$p'^* = \sqrt{\frac{2K_g R\gamma}{-\partial \hat{f} / \partial A_s}} \tag{66}$$

The reduction of $p'^*$ from 20 °C to 150 °C can be calculated by

$$\frac{p'^*_{150}}{p'^*_{20}} = \sqrt{\frac{\gamma_{150}}{\gamma_{20}}} = 0.83 \tag{67}$$

based on quartz parameters in Table 1.

Another observation from Figure 11 is that temperature affects the yield stresses more strongly in the high-pressure ductile region than in the low-pressure brittle region. This trend is also clear in the mean stress vs. porosity change data (Figure 12): thermal weakening is strongest at high confining pressures and diminishes rapidly as confining pressure decreases. Notably, the proposed SBM model together with Eq. (31) correctly predicted the shift in temperature sensitivity across low to high confining pressure in the yield surface and the stress-strain response of both sandstones. The agreement between model and data in the pre- and post-yielding regimes is also reasonably good, despite keeping all other parameters fixed. This provides another strong evidence that the observed thermal weakening is governed by the temperature dependence of surface energy $\gamma$, rather than by other properties such as stiffnesses $K$ and $G$, cohesion $c$, friction $M$, or hardening parameters $\omega$ and $s$.

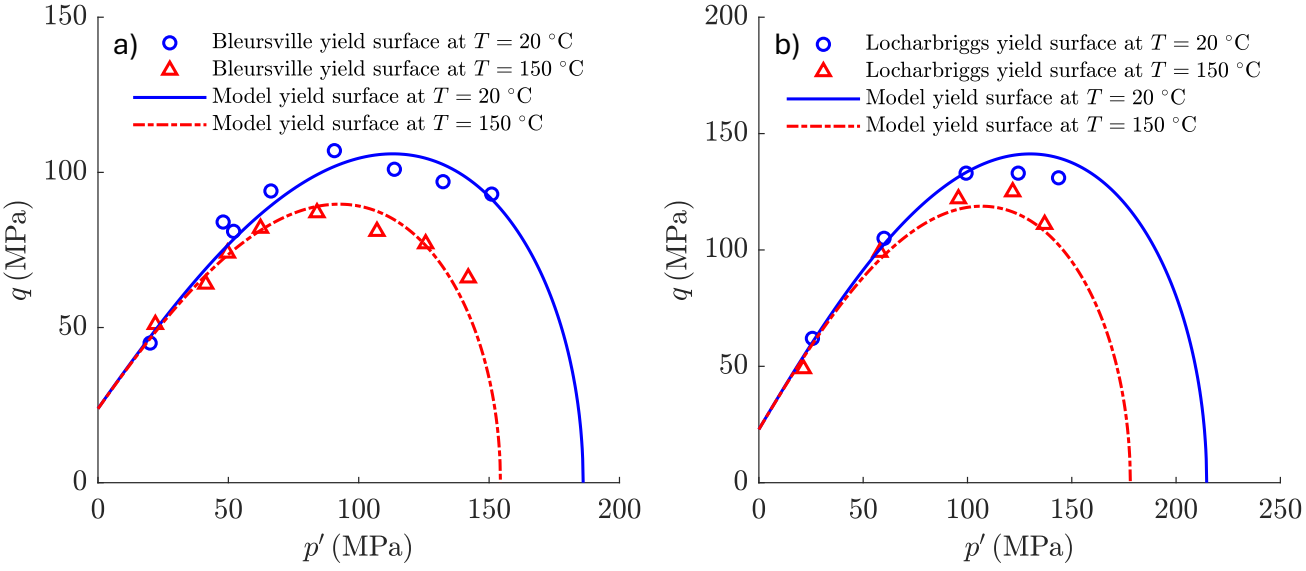


589

590 Figure 11: Yield surfaces for a) Bleursville sandstone and b) Locharbriggs sandstone at 20 and 150 °C.

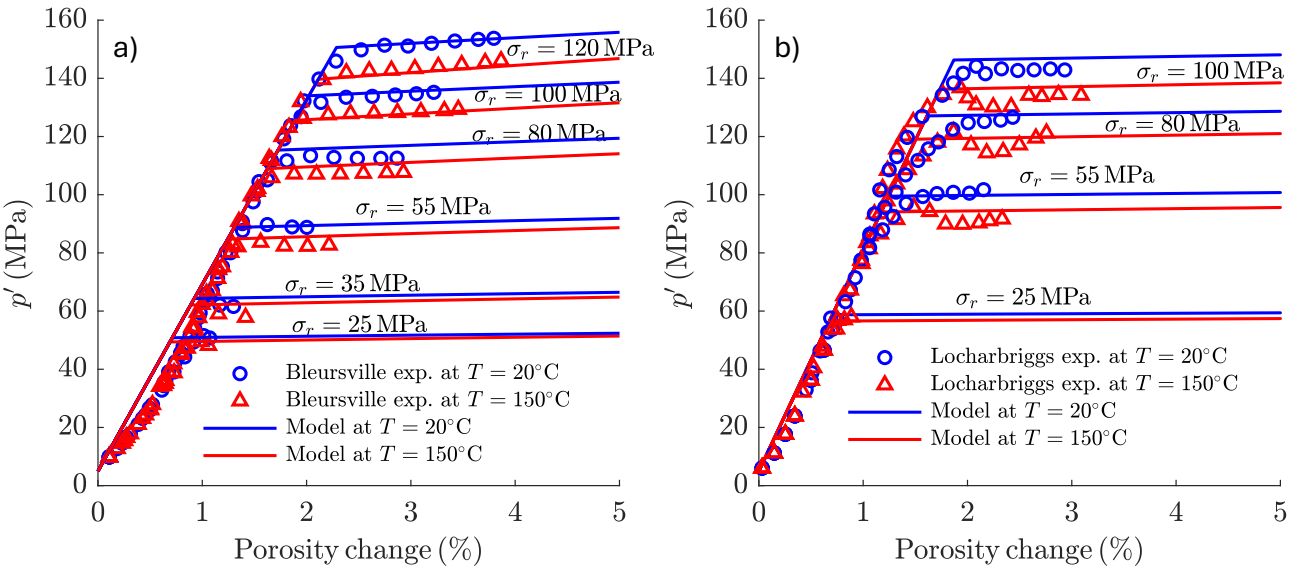


591

592 Figure 12: Effective mean stress ( $p'$ ) vs porosity change for a) Bleursville sandstone and b)
593 Locharbriggs sandstone at different confining pressures and at 20 and 150 °C.

594 ***4.2. Thermal weakening of St. Peter Sand***

595 Karner et al. (2003, 2005b, 2008) conducted triaxial compression tests on water-saturated St. Peter quartz

596 sand at 24 °C and 150 °C over a wide range of confining pressures, accompanied by acoustic emission

(AE) monitoring. The samples are characterized by an initially uniform GSD with grain size 250 - 350 $\mu$m, an average initial porosity 32.4%, and a minerology of nearly 100% quartz (Table 2). Similar to Section 4.1, the mechanical parameters of the St. Peter sand are calibrated with stress-strain data obtained at $T = 24$ °C, as listed in Table 3.

Figure 13 (a) shows the model performance for $q$ vs the porosity change at a confining pressure of 62.5 MPa at 24 and 150 °C. Again, the model accurately predicted the yielding and the stress-strain curve of St. Peter sand at the elevated temperature. The model captures well the measured mean stress vs. porosity change at 24 and 150 °C in Figure 13 (b), especially for the higher confining pressures. The elastic response again shows minimal temperature dependency similar to sandstone cases in Figure 12. The slight nonlinearity of the pre-yielding portion of the stress-strain curve exhibited in Figure 13 (b) can be better captured by adopting a nonlinear-elastic $\psi_r$ expression, as demonstrated elsewhere (Das et al., 2014; Kokash et al., 2024; Nguyen and Einav, 2009). Figure 14 shows the model yield surfaces at 24 and 150 °C, together with the experimental yield points reported by Karner et al. (2005; 2008). The model captures the experimental yield point reasonably well, with some mismatch in the lower confining pressure regime. Moreover, as observed for the sandstones, the thermal weakening of St. Peter sand becomes increasingly pronounced with increasing confining pressure. At low confinement, the mechanical behavior is governed primarily by friction between sand grains, which is consistent with the experimental observation that the yield points are largely insensitive to temperature (Karner et al., 2008). In contrast, at high confinement, the response is dominated by grain crushing (Karner et al., 2008), which is directly controlled by the surface energy $\gamma(T)$.

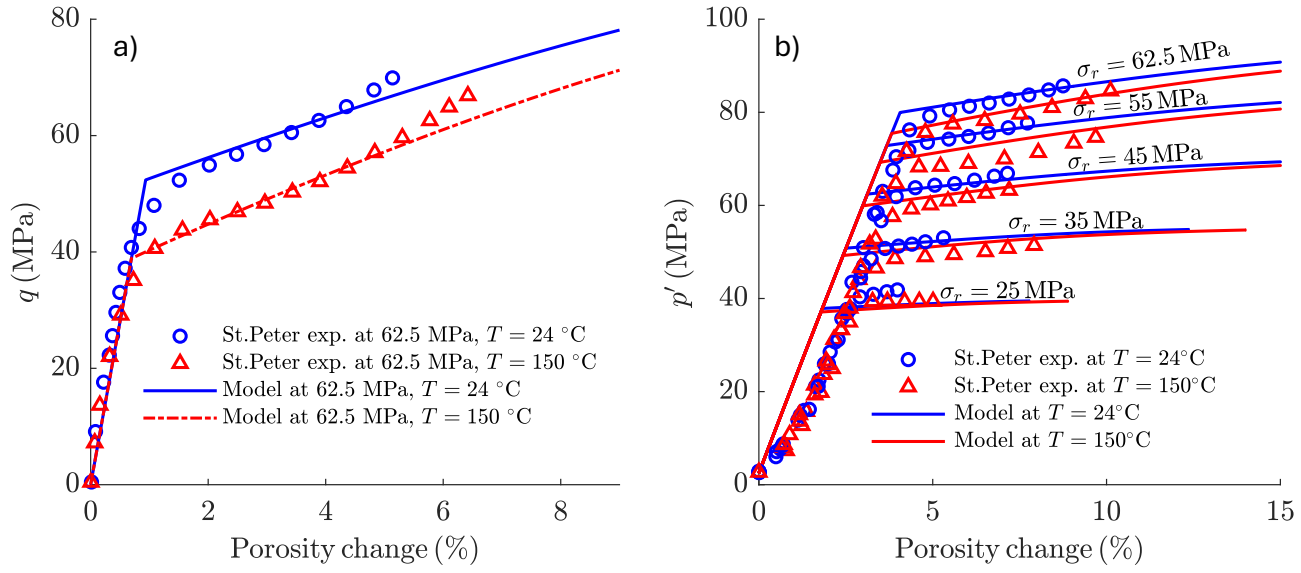


Figure 13: a) Deviatoric stress ( $q$ ) vs Porosity change for St. Peter sand at 62.5 MPa at 24, 150 °C; b) Effective mean stress ( $p'$ ) vs porosity change for St. Peter sand at different confining pressures and at 20 and 150 °C.

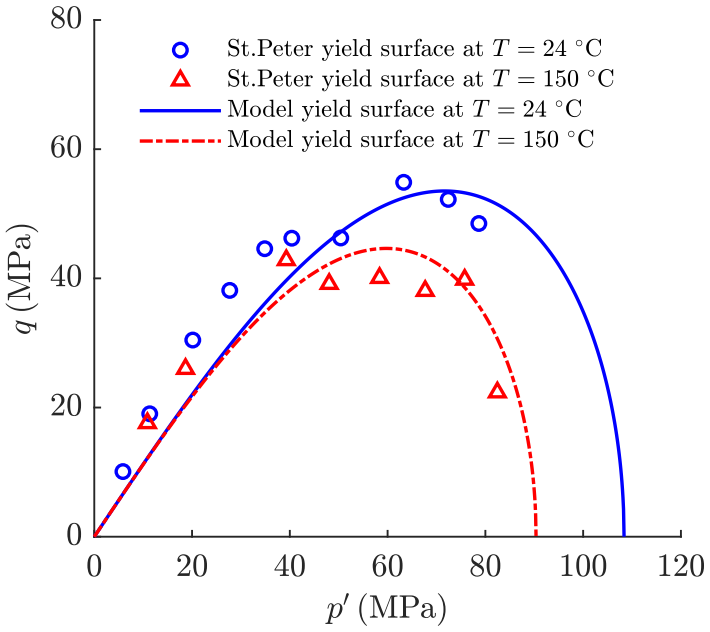


Figure 14: Yield surfaces for St. Peter sand at 24 and 150 °C. The experimental yield points were taken from the manual intersection of the ealstic and inelastic parts of the p vs pororotiy change curves in Karner et al. (2005; 2008)

In Karner et al.'s experimental campaign, several selected tests namely the 25, 62.5 and 87.5 MPa confining pressure at room temperature, and 55 MPa confining pressure at 150 °C, were instrumented with AE measurements (see Figure 16). AE represents grains fracture/ breakage and rises with increasing compression. In the current model, $A_s$ can be used to track the evolution of GSD through Eq. (49), enabling the subsequent computation of equivalent metrics for grain-crushing frequency. Figure 15 shows a schematic of two successive GSD curves at different $\chi$ values. The grain-size class that diminish can be referred to as 'parent grains', while new fragments appearing in smaller size fractions can be termed 'child grains'. The total number of parent grains crushed during an infinitesimal loading increment can be estimated by integrating the area between two successive GSDs from their intersection point to the maximum grain size (Figure 14), and combining this with the known total mass of the granular REV. Note that this calculation should be regarded only as a lower-bound approximation, because a given grain-size class may simultaneously lose parent grains to smaller size classes and receive daughter grains from larger ones. These two effects can partially cancel in the GSD-area difference, leading to an underestimation of the total number of grains that are actually crushed.

Figure 16 compares the total cumulative AE events and the cumulative number of parent grains obtained from the diminished area with respect to the porosity change for confining pressures of 25, 62.5 and 87.5 MPa at room temperature, and 55 MPa at 150 °C. We observe that the model-estimated cumulative number of parent grains shows good correspondence with the AE data: 1) the porosity change at the onset of massive grain crushing is correctly predicted for all samples tested at different confining pressures and temperatures, and 2) the evolution shape of the AE activity is consistent with that of the cumulative number of parent grains, supporting the proposed hardening function in Eq.(59). It is also noted that the modeled number of parent grains is about 0.3 – 0.6 times the measured number of AE events at the maximum experimental porosity change. This discrepancy is consistent with the argument above that the number of

parent grains inferred from the diminished GSD provides only a lower-bound estimate. Interestingly, for the test at 55 MPa and 150 $^{o}$C, the modeled number of parent grains matched the AE data.

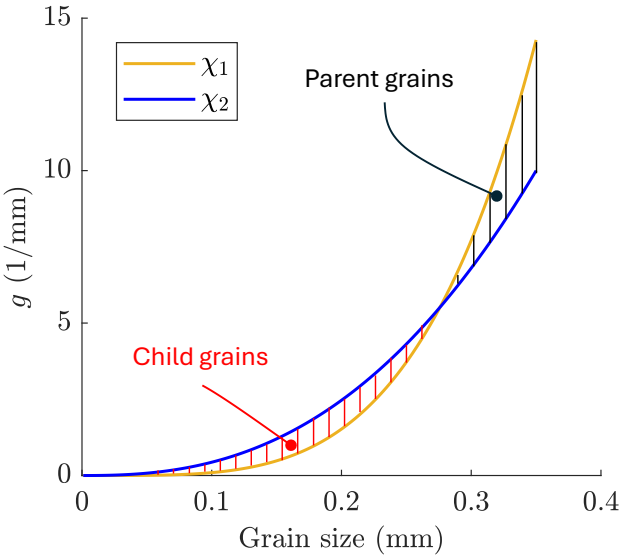


Figure 15: Schematic of probability grain size distribution by mass ( $g$ ) vs the grain size for two successive loadings at two different $\chi$ values, showing the areas that represents the parent and child grains.

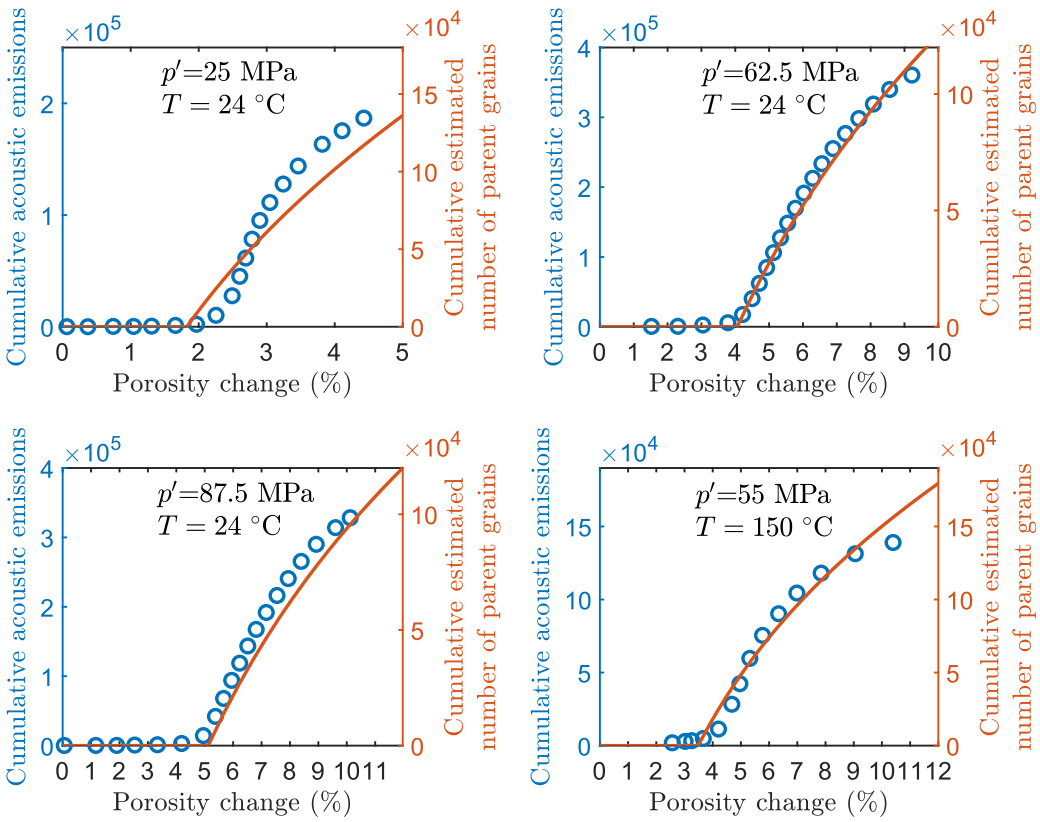


Figure 16: Measured cumulative AE data from Karner et al. (2003, 2005a, 2005b, 2008) and modeled cumulative number of parent grains for St. Peter sand, plotted as a function of porosity change, for confining pressures of 25, 62.5 and 87.5 MPa at $T = 24\,^{\circ}\mathrm{C}$ and 55 MPa at $T = 150\,^{\circ}\mathrm{C}$. The total mass was taken as 21.84 grams which corresponds to a cylindrical sample with a diameter of 19 mm and height of 43 mm (Karner et al., 2003), density of sand was taken as 2650 kg/m$^3$.

## 5. Discussions

### *5.1. The rearrangement factor R*

As mentioned earlier, $R$ amplifies the energy required to initiate grain crushing to account for energy needed to create new surface areas and and particle rearrangements within the granular assembly (Russell, 2011). The value of $R$ calibrated to match the yield stresses for Bleursville sandstone, Locharbriggs sandstone, and St. Peter quartz sand were 18.92, 3, and 57.5, respectively, as listed in Table 3. The

significantly higher value of $R$ for sand compared with sandstone is consistent with the fact that sand is cohesionless and lacks the intraparticle cementation present in sandstones, allowing grains greater freedom to redistribute. Russell (2011) comprehensively studied the energy dissipation of granular system undergoing a single particle crushing event and concluded the overall energy dissipation is proportional to surface energy $\gamma(1+\xi)$, where $\xi$ is the ratio of the redistribution dissipation to the surface-area-creation dissipation. The values of $\xi$ is expected to depend on the loading path and the boundary conditions (e.g., oedometric, triaxial, isotropic, etc.). Under oedometric compression, the values of $\xi$ are 13.4 and 15.4 for the two different particle sizes of the sand, where they have used a value of 25 $\mathrm{J/m^2}$ for $\gamma$. This is relatively high for the surface energy for quartz compared to the typical reported range of 0.28-11.5 $\mathrm{J/m^2}$ (Parks, 1984) and our selected value of 6 $\mathrm{J/m^2}$. For St. Peter sand, if we used their selected $\gamma$ of 25 $\mathrm{J/m^2}$, the corresponding value of $\xi$ would be 12.8, which is very close to those calculated in Russell (2011). Overall, the fact that *R* is significantly greater than 1 especially for uncemented sand indicates that the energy dissipated through grain rearrangement is substantially larger than that required for creating new surfaces at the onset of collective crushing.

### *5.2. Temperature weakening beyond 150 °C*

Outside the investigated temperature range of 20-150 °C, additional thermal effects may become significant and therefore can no longer be neglected as assumed in Eq. (67). Normalizing the isotropic crushing pressure ( $p'^{*}$ ) in Eq. (66) by its reference value at 20 °C gives:

$$\frac{p'^{*}}{p'^{*}_{20}} = \frac{\sqrt{\dfrac{2K_g R\gamma}{-\partial\hat{f}/\partial A_s}}}{\sqrt{\dfrac{2K_{g,20}R_{20}\gamma_{20}}{-\left(\partial\hat{f}/\partial A_s\right)_{20}}}} \tag{68}$$

Assuming the geometrical and rearrangement factors are independent of temperature, i.e., $R = R_{20}$ and $\partial \hat{f} / \partial A_s = \left(\partial \hat{f} / \partial A_s\right)_{20}$, we obtain:

$$\frac{p'^*}{p'^*_{20}} = \frac{\sqrt{K_g \gamma}}{\sqrt{K_{g,20} \gamma_{20}}} \tag{69}$$

Substituting Eq. (31) in (69) reveals the dependence of the crushing pressure on the intrinsic parameters of the granular assembly:

$$\frac{p'^*}{p'^*_{20}} = \sqrt{\frac{K_g}{K_{g,20}} \frac{E^{qz}}{E^{qz}_{20}} \frac{1}{(1+\alpha^{qz}\Delta T)(1+\beta^{qz}\Delta T)^2}} \tag{70}$$

where the superscript $qz$ refer to quartz. Eq. (70) indicates that $p'^*$ scales with both $K_g$ and $E^{qz}$ to the power of $1/2$, with $\alpha$ to the power of $-1/2$, and with $\beta$ to the power of -1. Furthermore, assuming Hertzian contacts, the bulk modulus ($K_g$) of the granular assembly can be shown to scale with the mineral elastic modulus $E$ according to (Agnolin and Roux, 2007; Mavko et al., 2020; Zhang et al., 2016):

$$K_g \sim \left(E^{qz}\right)^{2/3} \tag{71}$$

Substituting Eq. (71) in Eq. (70) gives:

$$\frac{p'^*}{p'^*_{20}} = \sqrt{\left(\frac{E^{qz}}{E^{qz}_{20}}\right)^{5/3} \frac{1}{(1+\alpha^{qz}\Delta T)(1+\beta^{qz}\Delta T)^2}} \tag{72}$$

Figure 17 (a) shows the predicted dependence of $p'^* / p'^*_{20}$ on temperature, with and without including the effect of $K_g(T)$, namely, using Eq. (70) with $K_g / K_{g,20} = 1$ and Eq. (72), respectively. Up to 200 °C, the influence of $K_g$ on $p^*$ is negligible, which is consistent with our previous conclusion that the thermal

weakening of sand and sandstone is primarily governed by surface energy reduction in the temperature range of 20-150 °C. Beyond 200 °C, the effect of $K_g$ becomes more pronounced.

Figure 17 (b) shows the predicted $p'^* / p'^*_{20}$ for different values of $\alpha$ and $\beta$. The results indicate that the crushing pressure is relatively insensitive to the thermal expansion coefficient, with only modernate variations even when $\alpha$ is assigned a much larger value. For example, the value of $p'^* / p'^*_{20}$ at 560 °C decreases by only a factor of 1.28 when $\alpha$ is increased by a factor of 100. By comparison, the $p'^* / p'^*_{20}$ curve is more sensitive to the decay length parameter. Specifically, changing $\beta$ from $0.5\beta^{qz}$ to $2\beta^{qz}$ (a factor of 4) leads to a decrease in $p'^* / p'^*_{20}$ at 560 °C by a factor of 1.86.

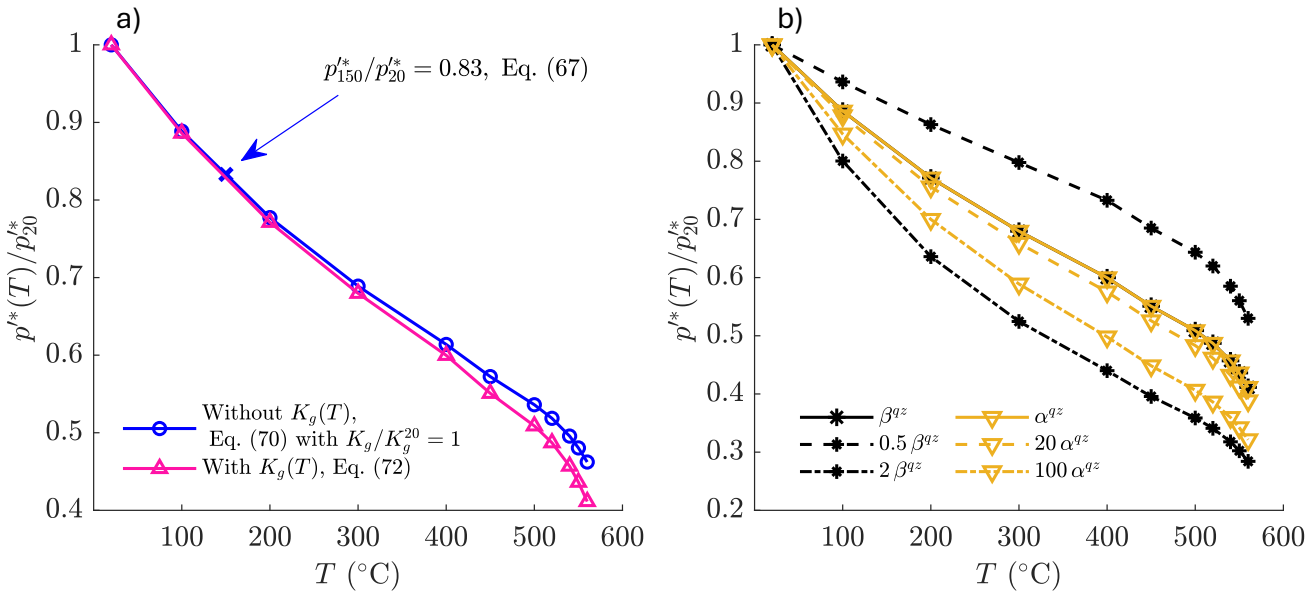


Figure 17: Predicted $p'^* / p'^*_{20}$ a) with and without considering the effect of $K_g(T)$; and b) under different values of $\alpha^{qz}$ and $\beta^{qz}$.

## 6. Conclusions

We present a bottom-up approach to understand and model the effect of temperature on yielding behavior on granular geomaterials. First, the atomic-scale origin of temperature-dependent fracture toughness of brittle minerals was investigated, leading to the development of an analytical model that relates surface energy to temperature. This important quantity was then integrated into continuum modeling of brittle granular materials through a thermodynamically consistent, surface-based breakage mechanics theory. A key innovation of the proposed theory compared to the conventional breakage mechanics is the use of specific surface area as the sole internal state variable to track the degree of grain crushing. Surface energy, as the thermodynamic conjugate of specific surface area, enters naturally into the dissipation rate function to modulate the yielding and hardening of the granular assembly. Additionally, we employed a fractal-type expression to relate the current GSD to the initial and ultimate GSDs. This approach more accurately captures the evolving GSD, especially in the fine-particle range, than the usual linear interpolation. The model performance was assessed by comparing its response with experimental data for Bleursville and Locharbriggs sandstones as well as St. Peter quartz sand. We showed that, by considering only the temperature dependence of quartz surface energy calibrated from mineral-scale fracture toughness tests, the surface-based breakage theory naturally reproduces the varying degrees of thermal weaking observed in these granular materials under different confining pressures. On the other hand, all materials exhibit negligible variation in elastic properties in the tested temperature range. These findings quantitatively suggest that the temperature dependence of bulk elasticity plays a secondary role compared to the reduction of surface energy, or equivalently the fracture toughness, of the constituent minerals in governing the thermal weakening of brittle granular materials.

It is worth noting that the above conclusion is validated for quartz-dominated granular materials in the studied temperature range. For more ductile grains (e.g., carbonates) or at higher temperatures near or beyond phase transitions, additional thermal weakening mechanisms such as increased dislocation

activity, plastic/viscoplastic flow, and fluid-induced dissolution, are likely to become important. The proposed theory provides a foundation for a wide range of generalizations. One promising direction is the modeling of the degradation of granular materials under coupled humidity and thermal effects, which frequently arise in applications such as dam engineering, pharmaceutical processing, and geothermal energy extraction. Furthermore, incorporating surface chemistry into the framework would enable systematic study of how pore-fluid chemistry influences the mechanical response of granular materials and geomaterials.

## Authorship contribution statement

Yazeed Kokash: Data curation, Investigation, Methodology, Visualization, Writing – original draft. Richard Regueiro: Project administration, Funding acquisition, Writing – review & editing . Yida Zhang: Conceptualization, Methodology, Supervision, Funding acquisition, Writing – review & editing.

## Declaration of competing interest

The authors declare that they have no known competing financial interests or personal relationships that could have appeared to influence the work reported in this paper.

## Acknowledgments

This research was funded by the U.S. National Science Foundation (NSF) under NSF CMMI Award No. 2237332, Predictive Science Academic Alliance Program (PSAAP) under Award DE-NA0003962, and DOE-BES-Geosciences program under Award DE-SC0024391.

## References

Agnolin, I., Roux, J.-N., 2007. Internal states of model isotropic granular packings. III. Elastic properties. Physical Review E 76, 061304.

Asay, J.R., Urzendowski, S., Guenther, A.H., 1968. Ultrasonic and thermal studies of selected plastics, laminated materials, and metals.

762 Ashari, S.E., Buscarnera, G., Cusatis, G., 2017. A lattice discrete particle model for pressure-dependent
763 inelasticity in granular rocks. International Journal of Rock Mechanics and Mining Sciences 91, 49-58.
764 Baraka-Lokmane, S., Main, I., Ngwenya, B., Elphick, S., 2009. Application of complementary methods
765 for more robust characterization of sandstone cores. Marine and Petroleum Geology 26, 39-56.
766 Bardet, J., Choucair, W., 1991. A linearized integration technique for incremental constitutive equations.
767 International Journal for Numerical and Analytical Methods in Geomechanics 15, 1-19.
768 Ben-Nun, O., Einav, I., 2010. The role of self-organization during confined comminution of granular
769 materials. Philosophical Transactions of the Royal Society A: Mathematical, Physical and Engineering
770 Sciences 368, 231-247.
771 Brandl, H., 2006. Energy foundations and other thermo-active ground structures. Geotechnique 56, 81-
772 122.
773 Buckman, S., Morris, R.H., Bourman, R.P., 2021. Fire-induced rock spalling as a mechanism of
774 weathering responsible for flared slope and inselberg development. Nature communications 12, 2150.
775 Buscarnera, G., Einav, I., 2021. The mechanics of brittle granular materials with coevolving grain size and
776 shape. Proceedings of the Royal Society A 477, 20201005.
777 Carr, D.D., 1971. Specialty sand resources of Indiana. Indiana Geological & Water Survey.
778 Cheng, Z., Wang, J., 2021. An investigation of the breakage behaviour of a pre-crushed carbonate sand
779 under shear using X-ray micro-tomography. Engineering Geology 293, 106286.
780 Chester, F., Chester, J., Kronenberg, A., Hajash, A., 2007. Subcritical creep compaction of quartz sand at
781 diagenetic conditions: Effects of water and grain size. Journal of Geophysical Research: Solid Earth 112.
782 Chester, J.S., Lenz, S.C., Chester, F.M., Lang, R., 2004. Mechanisms of compaction of quartz sand at
783 diagenetic conditions. Earth and Planetary Science Letters 220, 435-451.
784 Darot, M., Gueguen, Y., Benchemam, Z., Gaboriaud, R., 1985. Ductile-brittle transition investigated by
785 micro-indentation: results for quartz and olivine. Physics of the Earth and Planetary Interiors 40, 180-186.
786 Das, A., Tengattini, A., Nguyen, G.D., Viggiani, G., Hall, S.A., Einav, I., 2014. A thermomechanical
787 constitutive model for cemented granular materials with quantifiable internal variables. Part II–validation
788 and localization analysis. Journal of the Mechanics and Physics of Solids 70, 382-405.
789 Duggal, R., Rayudu, R., Hinkley, J., Burnell, J., Wieland, C., Keim, M., 2022. A comprehensive review
790 of energy extraction from low-temperature geothermal resources in hydrocarbon fields. Renewable and
791 Sustainable Energy Reviews 154, 111865.
792 Einav, I., 2007a. Breakage mechanics—part I: theory. Journal of the Mechanics and Physics of Solids 55,
793 1274-1297.
794 Einav, I., 2007b. Breakage mechanics—Part II: Modelling granular materials. Journal of the Mechanics
795 and Physics of Solids 55, 1298-1320.
796 Eppes, M.C., Keanini, R., 2017. Mechanical weathering and rock erosion by climate‐dependent
797 subcritical cracking. Reviews of Geophysics 55, 470-508.
798 Fadia, P., Tyagi, S., Bhagat, S., Nair, A., Panchal, P., Dave, H., Dang, S., Singh, S., 2021. Calcium
799 carbonate nano-and microparticles: synthesis methods and biological applications. 3 Biotech 11, 1-30.
800 Gao, S., Zhang, Y.D., Sonta, A., Buscarnera, G., 2016. Evolution of the water retention characteristics of
801 granular materials subjected to grain crushing. Journal of Geotechnical and Geoenvironmental
802 Engineering 142.
803 Gens, A., Sánchez, M., Guimarães, L.d.N., Alonso, E., Lloret, A., Olivella, S., Villar, M., Huertas, F.,
804 2009. A full-scale in situ heating test for high-level nuclear waste disposal: observations, analysis and
805 interpretation. Géotechnique 59, 377-399.
806 Gilman, J.J., 1960. Direct measurements of the surface energies of crystals. Journal of applied physics 31,
807 2208-2218.

Gkousis, S., Welkenhuysen, K., Compernolle, T., 2022. Deep geothermal energy extraction, a review on environmental hotspots with focus on geo-technical site conditions. Renewable and Sustainable Energy Reviews 162, 112430.
Heap, M., Baud, P., Meredith, P., 2009. Influence of temperature on brittle creep in sandstones. Geophysical Research Letters 36.
Houlsby, G.T., Puzrin, A.M., 2007. Principles of hyperplasticity: an approach to plasticity theory based on thermodynamic principles. Springer Science & Business Media.
Hueckel, T., Peano, A., Pellegrini, R., 1994. A thermo-plastic constitutive law for brittle-plastic behavior of rocks at high temperatures. pure and applied geophysics 143, 483-510.
Jefferd, M., Brantut, N., Meredith, P.G., Mitchell, T.M., Plümper, O., 2021. Compactive deformation of sandstone under crustal pressure and temperature conditions. Journal of Geophysical Research: Solid Earth 126, e2020JB020202.
Karner, S.L., Kronenberg, A.K., Chester, F.M., Chester, J.S., Hajash Jr, A., 2008. Hydrothermal deformation of granular quartz sand. Journal of Geophysical Research: Solid Earth 113.
Kelly, A., 1966. Strong Solids. Oxford University Press, Oxford, England.
Kokash, Y., Regueiro, R., Miller, N., Zhang, Y., 2024. A non-isothermal breakage-damage model for plastic-bonded granular materials incorporating temperature, pressure, and rate dependencies. International Journal of Solids and Structures, 113085.
Kranz, R.L., Harris, W.J., Carter, N.L., 1982. Static fatigue of granite at 200 C. Geophysical Research Letters 9, 1-4.
Lakshtanov, D.L., Sinogeikin, S.V., Bass, J.D., 2007. High-temperature phase transitions and elasticity of silica polymorphs. Physics and Chemistry of Minerals 34, 11-22.
Lawn, B., 2010. Fracture of brittle solids. Cambridge solid state science series.
Liu, L., Ji, H., Elsworth, D., Zhi, S., Lv, X., Wang, T., 2020. Dual-damage constitutive model to define thermal damage in rock. International Journal of Rock Mechanics and Mining Sciences 126, 104185.
Lobo-Guerrero, S., Vallejo, L.E., Vesga, L.F., 2006. Visualization of crushing evolution in granular materials under compression using DEM. International Journal of Geomechanics 6, 195-200.
López, J., Diosa, J., García, G., Mosquera, E., Correa, H., 2022. Temperature-dependent potential for the molecular dynamics of the superionic conductor β-PbF2. Heliyon 8.
Mavko, G., Mukerji, T., Dvorkin, J., 2020. The rock physics handbook. Cambridge university press.
McDowell, G., Bolton, M., 1998. On the micromechanics of crushable aggregates. Géotechnique 48, 667-679.
Meredith, P.G., 1983. A fracture mechanics study of experimentally deformed crustal rocks. University of London.
Meredith, P.G., Atkinson, B.K., 1982. High-temperature tensile crack propagation in quartz: Experimental results and application to time-dependent earthquake rupture. EPR. Earthquake prediction research 1, 377-391.
Monahan, J., Zhang, Y., Anderson, R.S., 2025. Spalling by repeated forest fires can mimic inselberg flared slope profiles. Journal of Geophysical Research: Earth Surface 130, e2025JF008628.
Nasehzadeh, A., Mohseni, M., Azizi, K., 2002. The effect of temperature on the Lennard–Jones (6–12) pair potential function. Journal of Molecular Structure: THEOCHEM 589, 329-335.
Nguyen, G.D., Einav, I., 2009. The energetics of cataclasis based on breakage mechanics. Pure and applied geophysics 166, 1693-1724.
Niemeijer, A., Spiers, C., Bos, B., 2002. Compaction creep of quartz sand at 400–600 C: Experimental evidence for dissolution-controlled pressure solution. Earth and Planetary Science Letters 195, 261-275.
Orowan, E., 1949. Fracture and strength of solids. Reports on progress in physics 12, 185.

Pabst, W., Gregorová, E., 2013. Elastic properties of silica polymorphs–a review. Ceramics-Silikaty 57, 167-184.
Parks, G.A., 1984. Surface and interfacial free energies of quartz. Journal of Geophysical Research: Solid Earth 89, 3997-4008.
Paterson, M.S., Wong, T.-f., 2005. Experimental rock deformation: the brittle field. Springer.
Punya-in, Y., Kongkitkul, W., 2023. Effects of temperature on the stress-strain-time behavior of sand under shear. Journal of Testing and Evaluation 51, 686-705.
Rice, J., 1978. Thermodynamics of the quasi-static growth of Griffith cracks. Journal of the Mechanics and Physics of Solids 26, 61-78.
Russell, A., 2011. A compression line for soils with evolving particle and pore size distributions due to particle crushing. Géotechnique Letters 1, 5-9.
Russell, A.R., Einav, I., 2013. Energy dissipation from particulate systems undergoing a single particle crushing event. Granular Matter 15, 299-314.
Sammis, C., King, G., Biegel, R., 1987. The kinematics of gouge deformation. Pure and Applied Geophysics 125, 777-812.
Shartsis, L., Spinner, S., 1951. Viscosity and density of molten optical glasses. Journal of Research of the National Bureau of Standards 46, 176-194.
Shinkai, N., Bradt, R., Rindone, G.E., 1981. Fracture toughness of fused SiO2 and float glass at elevated temperatures. Journal of the American Ceramic Society 64, 426-430.
Singh, S., Zurakowski, Z., Dai, S., Zhang, Y., 2021. Effect of grain crushing on the hydraulic conductivity of tailings sand. Journal of Geotechnical and Geoenvironmental Engineering 147, 04021143.
Sohn, C., Zhang, Y.D., Cil, M., Buscarnera, G., 2017. Experimental assessment of continuum breakage models accounting for mechanical interactions at particle contacts. Granular Matter 19.
Spinner, S., 1956. Elastic moduli of glasses at elevated temperatures by a dynamic method. Journal of the American Ceramic Society 39, 113-118.
Sutton, A.P., 1989. Temperature-dependent interatomic forces. Philosophical Magazine A 60, 147-159.
Wang, P., Karatza, Z., Arson, C., 2019. DEM modelling of sequential fragmentation of zeolite granules under oedometric compression based on XCT observations. Powder Technology 347, 66-75.
Wiederhorn, S., Johnson, H., Diness, A., Heuer, A., 1974. Fracture of glass in vacuum. Journal of the American Ceramic Society 57, 336-341.
Wiederhorn, S.M., 1969. Fracture surface energy of glass. Journal of the American Ceramic Society 52, 99-105.
Wong, T.-F., 1982. Effects of temperature and pressure on failure and post-failure behavior of Westerly granite. Mechanics of Materials 1, 3-17.
Xing, Y., Zhang, G., Li, S., 2020. Thermoplastic constitutive modeling of shale based on temperature-dependent Drucker-Prager plasticity. International Journal of Rock Mechanics and Mining Sciences 130, 104305.
Zeidler, A., Salmon, P.S., Usuki, T., Kohara, S., Fischer, H.E., Wilson, M., 2022. Structure of molten NaCl and the decay of the pair-correlations. The Journal of Chemical Physics 157.
Zhang, C., Nguyen, G., Einav, I., 2013. The end-bearing capacity of piles penetrating into crushable soils. Géotechnique 63, 341.
Zhang, Y., 2018. Mechanics of adsorption-deformation coupling in porous media. Journal of the Mechanics and Physics of Solids 114, 31-54.
Zhang, Y., Buscarnera, G., 2014. Grainsize dependence of clastic yielding in unsaturated granular soils. Granular Matter 16, 469-483.

Zhang, Y., Buscarnera, G., 2018. Breakage mechanics for granular materials in surface-reactive environments. Journal of the Mechanics and Physics of Solids 112, 89-108.
Zhang, Y.D., Buscarnera, G., Einav, I., 2016. Grain size dependence of yielding in granular soils interpreted using fracture mechanics, breakage mechanics and Weibull statistics. Geotechnique 66, 149-160.
Zhou, X., Ma, G., Zhang, Y., 2019. Grain size and time effect on the deformation of rockfill dams: a case study on the Shuibuya CFRD. Géotechnique 69, 606-619.
Ziegler, H., 1977. An introduction to thermodynamics. North-Holland Publishing Company.
Ziegler, H., 1983. An Introduction to Thermomechanics, 2nd ed. North-Holland Publishing Company, Netherlands.

## Appendix

The incremental constitutive relations written in matrix form are:

$$\begin{pmatrix} \dot{p} \\ \dot{q} \\ -\dot{S} \end{pmatrix} = \overbrace{\left[\mathbf{D}^e - \mathbf{D}^P - \mathbf{D}^A\right]}^{\left[\mathbf{D}^{ePA}\right]} \begin{pmatrix} \dot{\varepsilon}_v \\ \dot{\varepsilon}_s \\ \dot{T} \end{pmatrix} \tag{A.1}$$

where

$$\left[\mathbf{D}^e\right] = \begin{bmatrix} \alpha_{vv} & \alpha_{vs} & \alpha_{vT} \\ \alpha_{vs} & \alpha_{ss} & \alpha_{sT} \\ \alpha_{vT} & \alpha_{sT} & \alpha_{TT} \end{bmatrix} \tag{A.2}$$

$$\left[\mathbf{D}^p\right] = \frac{1}{K_{PA}} \begin{bmatrix} \left(\alpha_{vv}\frac{\partial \overline{y}}{\partial \overline{p}} + \alpha_{vs}\frac{\partial \overline{y}}{\partial \overline{q}}\right)\xi_v & \left(\alpha_{vv}\frac{\partial \overline{y}}{\partial \overline{p}} + \alpha_{vs}\frac{\partial \overline{y}}{\partial \overline{q}}\right)\xi_s & \left(\alpha_{vv}\frac{\partial \overline{y}}{\partial \overline{p}} + \alpha_{vs}\frac{\partial \overline{y}}{\partial \overline{q}}\right)\xi_T \\ \left(\alpha_{vs}\frac{\partial \overline{y}}{\partial \overline{p}} + \alpha_{ss}\frac{\partial \overline{y}}{\partial \overline{q}}\right)\xi_v & \left(\alpha_{vs}\frac{\partial \overline{y}}{\partial \overline{p}} + \alpha_{ss}\frac{\partial \overline{y}}{\partial \overline{q}}\right)\xi_s & \left(\alpha_{vs}\frac{\partial \overline{y}}{\partial \overline{p}} + \alpha_{ss}\frac{\partial \overline{y}}{\partial \overline{q}}\right)\xi_T \\ \left(\alpha_{vT}\frac{\partial \overline{y}}{\partial \overline{p}} + \alpha_{sT}\frac{\partial \overline{y}}{\partial \overline{q}}\right)\xi_v & \left(\alpha_{vT}\frac{\partial \overline{y}}{\partial \overline{p}} + \alpha_{sT}\frac{\partial \overline{y}}{\partial \overline{q}}\right)\xi_s & \left(\alpha_{vT}\frac{\partial \overline{y}}{\partial \overline{p}} + \alpha_{sT}\frac{\partial \overline{y}}{\partial \overline{q}}\right)\xi_T \end{bmatrix} \tag{A.3}$$

$$\left[\mathbf{D}^A\right] = -\frac{1}{K_{PA}}\frac{\partial \overline{y}}{\partial \overline{E}_s} \begin{bmatrix} \alpha_{Av}\xi_v & \alpha_{Av}\xi_s & \alpha_{Av}\xi_T \\ \alpha_{As}\xi_v & \alpha_{As}\xi_s & \alpha_{As}\xi_T \\ \alpha_{AT}\xi_v & \alpha_{AT}\xi_s & \alpha_{AT}\xi_T \end{bmatrix} \tag{A.4}$$

$$K_{PA} = \xi_v\frac{\partial \overline{y}}{\partial \overline{p}} + \xi_s\frac{\partial \overline{y}}{\partial \overline{q}} - \xi_{A_s}\frac{\partial \overline{y}}{\partial \overline{E}_s} \tag{A.5}$$

$$\alpha_{vv} = \hat{f}\frac{\partial^2\psi_r}{\partial\varepsilon_v^{e2}};\alpha_{vs} = \hat{f}\frac{\partial^2\psi_r}{\partial\varepsilon_v^e\partial\varepsilon_s^e};\alpha_{vT} = \hat{f}\frac{\partial^2\psi_r}{\partial\varepsilon_v^e\partial T}$$

$$\alpha_{vA} = \frac{\partial\hat{f}}{\partial\chi}\frac{\partial\chi}{\partial A_s}\frac{\partial\psi_r}{\partial\varepsilon_v^e};\alpha_{ss} = \hat{f}\frac{\partial^2\psi_r}{\partial\varepsilon_s^{e2}};\alpha_{sT} = \hat{f}\frac{\partial^2\psi_r}{\partial\varepsilon_s^e\partial T} \tag{A.6}$$

$$\alpha_{sA} = \frac{\partial\hat{f}}{\partial\chi}\frac{\partial\chi}{\partial A_s}\frac{\partial\psi_r}{\partial\varepsilon_s^e};\alpha_{TT} = \hat{f}\frac{\partial^2\psi_r}{\partial T^2};\alpha_{AT} = \hat{f}\frac{\partial^2\psi_r}{\partial A\partial T}$$

$$\xi_v = \frac{\partial y}{\partial p}\left(\hat{f}\frac{\partial^2\psi_r}{\partial\varepsilon_v^{e2}}\right) + \frac{\partial y}{\partial q}\left(\hat{f}\frac{\partial^2\psi_r}{\partial\varepsilon_s^e\partial\varepsilon_v^e}\right) - \frac{\partial y}{\partial E_s}\left(\frac{\partial\hat{f}}{\partial\chi}\frac{\partial\chi}{\partial A_s}\frac{\partial\psi_r}{\partial\varepsilon_v^e}\right)$$

$$\xi_s = \frac{\partial y}{\partial p}\left(\hat{f}\frac{\partial^2\psi_r}{\partial\varepsilon_v^e\partial\varepsilon_s^e}\right) + \frac{\partial y}{\partial q}\left(\hat{f}\frac{\partial^2\psi_r}{\partial\varepsilon_s^{e2}}\right) - \frac{\partial y}{\partial E_s}\left(\frac{\partial\hat{f}}{\partial\chi}\frac{\partial\chi}{\partial A_s}\frac{\partial\psi_r}{\partial\varepsilon_s^e}\right)$$

$$\xi_{A_s} = \frac{\partial y}{\partial p}\left(\frac{\partial\hat{f}}{\partial\chi}\frac{\partial\chi}{\partial A_s}\frac{\partial\psi_r}{\partial\varepsilon_v^e}\right) + \frac{\partial y}{\partial q}\left(\frac{\partial\hat{f}}{\partial\chi}\frac{\partial\chi}{\partial A_s}\frac{\partial\psi_r}{\partial\varepsilon_s^e}\right) + \frac{\partial y}{\partial A_s} - \frac{\partial y}{\partial E_s}\psi_r\left[\frac{\partial\hat{f}}{\partial\chi}\frac{\partial^2\chi}{\partial A_s^2} + \left(\frac{\partial\chi}{\partial A_s}\right)^2\frac{\partial^2\hat{f}}{\partial\chi^2}\right] \tag{A.7}$$

$$\xi_T = \frac{\partial y}{\partial p}\left(\hat{f}\frac{\partial^2\psi_r}{\partial\varepsilon_v^e\partial T}\right) + \frac{\partial y}{\partial q}\left(\hat{f}\frac{\partial^2\psi_r}{\partial\varepsilon_s^e\partial T}\right) - \frac{\partial y}{\partial E_s}\frac{\partial\hat{f}}{\partial\chi}\frac{\partial\chi}{\partial A_s}\frac{\partial\psi_r}{\partial T} + \frac{\partial y}{\partial T}$$

The plastic multiplier, $\lambda$, is given by:

$$\lambda = \frac{\xi_v\dot{\varepsilon}_v + \xi_s\dot{\varepsilon}_s + \xi_T\dot{T}}{K_{PA}} \tag{A.8}$$

The constitutive equations are implemented in a material-point driver in MATLAB. The equations were integrated using an explicit substepping scheme.

Arbitrary mixed strain-stress control is realized through the method of Bardet and Choucair (1991). Specifically, each mixed control loading increment can be written as:

$$[\mathbf{S}](\dot{\boldsymbol{\sigma}}) + [\mathbf{E}](\dot{\boldsymbol{\varepsilon}}) = (\dot{\mathbf{X}}) \tag{A.9}$$

where $[\mathbf{S}]$ and $[\mathbf{E}]$ are the stress and strain constraint matrices, respectively; $(\dot{\boldsymbol{\sigma}})$ and $(\dot{\boldsymbol{\varepsilon}})$ are the stress and strain increment vectors, respectively; and $(\dot{\mathbf{X}})$ is the drive vector. For example, the constraint matrices and drive vector for an isothermal, strain driven, drained triaxial compression test is given by:

$$[\mathbf{S}]=\begin{bmatrix}-3 & 1 & 0\\ 0 & 0 & 0\\ 0 & 0 & 0\end{bmatrix},\ [\mathbf{E}]=\begin{bmatrix}0 & 0 & 0\\ 0 & 1 & 0\\ 0 & 0 & 0\end{bmatrix},\ (\dot{\mathbf{X}})=\begin{pmatrix}0\\ \dot{X}\\ 0\end{pmatrix} \tag{A.10}$$

During a plastic load step, we have $(\dot{\boldsymbol{\sigma}})=\left[\mathbf{D}^{ePA}\right](\dot{\boldsymbol{\varepsilon}})$ where $\left[\mathbf{D}^{ePA}\right]$ is the elastoplastic constitutive matrix in Eq. (A.1). Substitution this into Eq. (A.9) gives:

$$\underbrace{\left([\mathbf{S}]\left[\mathbf{D}^{ePA}\right]+[\mathbf{E}]\right)}_{[\mathbf{A}]}(\dot{\boldsymbol{\varepsilon}})=(\dot{\mathbf{X}}) \tag{A.11}$$

From Eq. (A.11), the strain increment can be calculated as:

$$(\dot{\boldsymbol{\varepsilon}})=[\mathbf{A}]^{-1}(\dot{\mathbf{X}}) \tag{A.12}$$

Eq. (A.12) essentially convert every mixed control test into a strain-controlled test within an explicit integration schemes. It is therefore especially convenient for material-point drivers used to inspect constitutive responses before full-fledged finite element implementation.